

# Probing the Protostellar Envelope around L1157: the Dust and Gas Connection

Hsin-Fang Chiang<sup>1</sup>, Leslie W. Looney<sup>1</sup>, John J. Tobin<sup>2</sup>, Lee Hartmann<sup>2</sup>

## ABSTRACT

We present observations of the Class 0 protostar L1157-mm using the Combined Array for Research in Millimeter-wave Astronomy (CARMA) in 3 mm dust continuum and  $\text{N}_2\text{H}^+$  line emission. In the  $\text{N}_2\text{H}^+$  line, we detect a large-scale envelope extended over a linear size of  $\sim 20,000\text{AU}$  flattened in the direction perpendicular to the outflow. This  $\text{N}_2\text{H}^+$  feature coincides with the outer envelope seen in the  $8\ \mu\text{m}$  extinction by Looney et al. Meanwhile, the dust continuum traces the compact, nearly spherical structure of the inner envelope, where  $\text{N}_2\text{H}^+$  becomes depleted. This highly flattened  $\text{N}_2\text{H}^+$  envelope also shows dynamical signatures consistent with gravitational infall in the inner region, but a slow, solid-body rotation at large scales. This flattened structure is not a rotationally supported circumstellar disk; instead, it resembles a prestellar core both morphologically and kinematically, representing the early phase of a Class 0 system. In this paper, we construct a simple model to interpret both the dust continuum and  $\text{N}_2\text{H}^+$  emission and suggest a possible dynamical scenario for the overall properties of the envelope.

*Subject headings:* stars: formation — techniques: interferometric — ISM: molecules — stars: individual (L1157) —

## 1. Introduction

Significant progress has been made both theoretically and observationally toward understanding low-mass star formation in the last few decades, and an evolutionary sequence has been posited (e.g., Andre et al. 2000; McKee & Ostriker 2007; Evans et al. 2009). The youngest protostars, the so-called Class 0 sources, form from the preceding stage of a prestellar core and are deeply embedded in their natal collapsing envelope. As a link from prestellar cores to young protostars, these envelopes contain valuable physical clues to the initial conditions of the collapse process. While single-dish telescope observations alone are usually limited by large beam size, interferometry has allowed high resolution studies of the Class 0 envelope. In particular, interferometric observations combined with dust modeling using theoretically predicted structure can probe the physical

---

<sup>1</sup>Department of Astronomy, University of Illinois at Urbana-Champaign, 1002 West Green Street, Urbana, IL 61801; hchiang2@uiuc.edu

<sup>2</sup>Department of Astronomy, University of Michigan, Ann Arbor, MI 48109

properties of the inner envelope (e.g., Looney et al. 2003; Chiang et al. 2008). Unfortunately, dust emission from the outer envelope is usually difficult to detect due to interferometer insensitivity to the large-scale structure or the low-surface brightness of the extended emission. Molecular lines, on the other hand, trace specific components of the envelope and can detect regions of lower density. Further, as the line emission is dispersed over many velocity channels, the structures are less extended than the equivalent dust emission so less affected by interferometer resolving-out issues. However, uncertainty in abundances and chemistry in the envelope can make molecular line interpretation difficult.

Since the first detection in Turner (1974) and confirmation in Thaddeus & Turner (1975),  $\text{N}_2\text{H}^+$  has been a well-known interstellar molecule and an excellent tracer of dense cores (e.g., Caselli et al. 2002; Chen et al. 2007). With a critical density of around  $10^5 \text{ cm}^{-3}$  (e.g., Daniel et al. 2006),  $\text{N}_2\text{H}^+$  is sensitive to the outer envelope around Class 0 young stellar objects (YSOs). Also,  $\text{N}_2\text{H}^+$  has a low depletion rate and remains in the gas phase when other molecules such as CO have depleted onto grains (Bergin & Langer 1997). The reason for this was thought to be the low binding energy of its parent molecule  $\text{N}_2$ , but recent experiments have shown that the binding energy of  $\text{N}_2$  is not much lower than that of CO (Öberg et al. 2005). In fact, most of the nitrogen is in the atomic form, which has a binding energy lower than the molecular form, and therefore making  $\text{N}_2\text{H}^+$  harder to deplete (Maret et al. 2006). In this paper, we use  $\text{N}_2\text{H}^+$  as an envelope tracer to reveal the gas in the outer protostellar envelope, as well as pursue a comparison between gas and dust.

While most Class 0 protostellar envelopes have rather complex structures, L1157-mm (also known as L1157-IRS or IRAS 20386+6751) in the Cepheus flare (e.g., Kun et al. 2008; Kirk et al. 2009) has a highly flattened and relatively symmetric envelope  $2'$  across seen by  $8 \mu\text{m}$  absorption (Looney et al. 2007; Tobin et al. 2009). The protostar is in the Class 0 stage with an estimated age of 8-150 kyr (Froebrich 2005, based on bolometric temperature, bolometric luminosity, and submillimeter luminosity). Different components of the dust emission, including a central compact core and an extended envelope, have been observed (e.g., Gueth et al. 1997, 2003; Beltrán et al. 2004). Also, large-scale outflows have been detected by various molecules, suggesting an inclination angle of  $80^\circ$  (Gueth et al. 1996) and a kinematic age of 15 kyr derived from the oldest pair of outflow clumps (Bachiller et al. 2001; Arce et al. 2008, and reference therein). Furthermore, detection of methanol has suggested active accretion in the embedded circumstellar disk (Goldsmith et al. 1999; Velusamy et al. 2002). With features of a typical Class 0 young stellar object, L1157 seems to be a good example of isolated low-mass star formation.

Unfortunately, the distance to L1157 is uncertain. The distance of 440 pc, based on spectroscopy and photometry of the illuminating star HD200775 of NGC 7023, is commonly used (see Kun et al. 2008), while the distance of the neighboring L1147/L1158 complex was determined to be 325 pc by the extinction-distance relationship in Straizys et al. (1992). Later, the Cepheus cloud was found to have three characteristic distances 200 pc, 300 pc, and 450 pc in Kun (1998). Multiple layers of clouds make it difficult to know the exact distance to a specific region. For easier

comparison with the study of Looney et al. (2007), we adopt 250 pc in this paper.

We present interferometric observations of L1157-mm using the Combined Array for Research in Millimeter-wave Astronomy (CARMA; Bock et al. 2006)<sup>1</sup>. The dust continuum at 3 mm and the N<sub>2</sub>H<sup>+</sup> gas emission are observed and studied. The observational setup and the results are presented in §2 and §3. We estimate the column density of the N<sub>2</sub>H<sup>+</sup> emission (§4.1) and compare it with the previous detection of the flattened envelope at 8 μm absorption (§4.2). The N<sub>2</sub>H<sup>+</sup> abundance is examined in §4.3. We construct a simple model to interpret both the dust continuum and the N<sub>2</sub>H<sup>+</sup> gas emission in §4.4. In addition, the gas kinematics of the large-scale envelope is discussed in §4.5. An overall link between gas and dust at multiple scales in this system is concluded in §4.6, following by a summary in §5.

## 2. Observations

The observations were carried out with CARMA in October 2008 in E configuration and March 2009 in D configuration. The system temperature ranged from 150 to 300K (single sideband, SSB) during source observations. D and E configurations are the two most compact configurations of CARMA and give angular resolutions of around 5.5'' and 10'' at 3 mm, respectively. Because of the short antenna separations (8-66 m) in E configuration, antennas can shadow each other when observing targets at low elevations. To minimize shadowing, the elevations were always above 30° throughout the observations. Also we checked and verified that no shadowed data of the source were included in the analysis.

CARMA is composed of nine 6.1m Berkeley Illinois Maryland Association (BIMA) antennas and six 10.4m Owens Valley Radio Observatory (OVRO) antennas<sup>2</sup>. At our observed frequency, the FWHM of the primary beams are 122'' and 70'' for the 6m and 10m dishes, corresponding to 30,500AU and 17,500AU, respectively. The sensitivity decreases significantly outside the FWHM. To observe the extended feature of L1157, we performed a five-pointing mosaic observation across the disk-like structure found in Looney et al. (2007). The phase center of the central pointing is set at the position of the protostar,  $\alpha = 20^h39^m06^s.26$  and  $\delta = 68^\circ02'15''.8$ , determined by the dust continuum peak from other high resolution CARMA observations (Chiang et al. in preparation).

The correlator was set so that the N<sub>2</sub>H<sup>+</sup>  $JF_1F=101-012$  component at 93.1763 GHz was observed with a 2 MHz bandwidth, which provided a velocity resolution of 0.098 km s<sup>-1</sup>. Dust continuum was observed simultaneously with two 500 MHz bands. During the observations, 1927+739 was observed every 18 minutes and used as the phase calibrator. Also, the bandpass calibrators were 3C454.3, 3C84, 3C345, and 1642+689 for different tracks, while the flux calibrators were Uranus and MWC349. The absolute flux uncertainty is around 10%; hereafter we only consider

---

<sup>1</sup><http://www.mmarray.org>

<sup>2</sup>Currently eight 3.5 m antennas from Sunyaev-Zeldovich Array (SZA) are also combined with CARMA

the statistical uncertainty. All observational data were reduced and imaged using the MIRIAD software package (Sault et al. 1995)<sup>3</sup>. For the maps shown in this paper, natural weighting is used for Fourier transforming the visibilities into the image space.

### 3. Results

#### 3.1. Dust Continuum

Figure 1(a) shows the 3 mm dust continuum map. With a beam size of  $7.3'' \times 6.5''$  (1825 AU  $\times$  1625 AU) in the combined D- and E-array CARMA data, the dust emission is compact and nearly spherical. We used the MIRIAD task IMFIT to fit the dust emission with a Gaussian, and the results are given in Table 1. We detect the spherical protostellar envelope, but the embedded early circumstellar disk is not resolved. The dust continuum seen by CARMA is more compact than that seen by single-dish observations (e.g., 850  $\mu$ m and 1.3 mm maps in Shirley et al. 2000; Gueth et al. 2003), implying that the large-scale extended emission is resolved out by the interferometer. A more careful modeling of the dust envelope is done in §4.4.

#### 3.2. N<sub>2</sub>H<sup>+</sup> Gas

Figures 1(b) and 2 show the integrated intensity (zeroth moment map) and the velocity channel maps of the N<sub>2</sub>H<sup>+</sup> isolated hyperfine component  $JF_1F=101-012$ . The star marks the position of the central protostar. We detect large-scale N<sub>2</sub>H<sup>+</sup> emission across an elongated region perpendicular to the outflow direction (see the gray-scale image in Figure 3(a) for the outflow orientation). The disk-like structure extends over  $80''$ , which corresponds to a linear size of  $\sim 20,000$  AU assuming a distance of 250 pc. Due to the large size, it is unlikely to be a rotationally supported disk (see §4.5.2). Hence, we call it a flattened envelope in this paper.

The N<sub>2</sub>H<sup>+</sup> gas shows interesting dynamics of the flattened envelope in Figure 2. Systematically, the east wing has lower velocity than the west wing, suggesting rotation or bulk motion. The dynamics of the system will be discussed more in later sections. The spatial distribution is clumpy. In particular, the extended emission toward the east-south roughly follows the interface of the envelope and outflow cavity, suggesting dynamical or chemical interaction between outflow and envelope. The effects of outflows on the morphology of N<sub>2</sub>H<sup>+</sup> emission are also seen in other YSOs (e.g., Chen et al. 2008). In addition, the emission extends to the very west of the observational field of view and becomes blended with noise. In this study we do not consider the western clumps (see Figure 1(b)); instead, we focus on the main part of the flattened envelope.

---

<sup>3</sup><http://carma.astro.umd.edu/miriad>

## 4. Analysis and Discussion

### 4.1. The Column Density of the N<sub>2</sub>H<sup>+</sup> Feature

The N<sub>2</sub>H<sup>+</sup> molecule (diazenylium) has 15  $J=1-0$  rotational transitions; spectroscopically, seven sets of hyperfine components are observed because the lower state energy levels  $J=0$  are degenerate within  $10^{-6}$  Hz (e.g., Daniel et al. 2006). The relative rest frequencies of the components were determined by Caselli et al. (1995). The so-called isolated component, the  $JF_1F=101-012$  component together with  $JF_1F=101-010$  and  $101-011$  at 93.176258 GHz (Lee et al. 2001), is not blended with the other sets of hyperfine components and is ideal for studying dynamics. We perform spectrum fitting for pixels with more than three S/N detection of N<sub>2</sub>H<sup>+</sup> on the integrated intensity map, except the very west region close to the edge of the field of view, where the spectrum fitting fails to be reliable. For simplicity, we assume a uniform excitation temperature  $T_{ex} = 10$  K with the local thermodynamic equilibrium (LTE) approximation for the level populations. Also, Gaussian lines with the same line width are used (cf. GILDAS CLASS HFS procedure <sup>4</sup> and Shirley et al. 2005). The isolated component accounts for a ratio of 3/27 of the total N<sub>2</sub>H<sup>+</sup> emission (Daniel et al. 2006), with which we convert our observed data to total emission accordingly. Then we calculated the best fit values of opacity  $\langle \tau \rangle$  (average  $\tau$  among seven hyperfine sets, see Shirley et al. 2005), FWHM of velocity dispersion  $\Delta v$ , and  $v_{\text{LSR}}$  for each pixel using the MATLAB function *nlinfit* <sup>5</sup>. A summary of the spectrum fitting as well as the uncertainty of fitting is in Table 2. In the optically thin limit and with the LTE assumption, the column density can be estimated with (Miao et al. 1995; Goldsmith & Langer 1999)

$$\mathcal{N}_{tot} = 2.04 \frac{Q(T_{ex}) e^{\frac{E_u}{kT_{ex}}}}{\theta_a \theta_b \nu^3 \mu^2 S} \left[ \frac{B_\nu(T_{ex})}{B_\nu(T_{ex}) - B_\nu(T_{bg})} \right] C_\tau \int I_\nu dv \times 10^{20} \text{cm}^{-2} \quad , \quad (1)$$

where  $\theta_a$  and  $\theta_b$  are observational beam size in arcsecond,  $\nu$  is the frequency in GHz,  $\mu$  is the dipole moment in debye,  $S$  is the line strength,  $E_u$  is the upper state energy level,  $B_\nu(T)$  is the Planck function at temperature  $T$ ,  $I_\nu$  is the specific intensity in Jy beam<sup>-1</sup>,  $v$  is velocity in km s<sup>-1</sup>,  $C_\tau$  is the opacity correction factor

$$C_\tau = \frac{\tau}{1 - e^{-\tau}} \quad , \quad (2)$$

$Q(T_{ex})$  is the rotational partition function

$$Q_{rot}(T_{ex}) = \sum_{J=0}^{\infty} (2J+1) e^{-\frac{E_J}{kT_{ex}}} \approx \frac{kT_{ex}}{hB} \quad (3)$$

(Goldsmith & Langer 1999),  $E_J = J(J+1)hB$  is the energy level for the rotational transition, and  $B$  is the rotational constant. For linear molecule N<sub>2</sub>H<sup>+</sup>,  $\mu$  is 3.40 debye and  $B$  is 46586.867 MHz

---

<sup>4</sup><http://www.iram.fr/IRAMFR/GILDAS/>

<sup>5</sup><http://www.mathworks.com/>

(JPL catalog: Pickett et al. 1998; Green et al. 1974). Since the emission is more extended than the beam size, the beam filling factor is assumed to be 1 across the map. Also, the background temperature  $T_{bg}$  is assumed to be constant 2.73K.

Altogether, the estimated  $N_2H^+$  column density is shown by the dark contours in Figure 3, with the velocity map shown in colormap in Figure 3(b). The average column density is  $\sim 1.0 \times 10^{13} \text{cm}^{-2}$  with a peak of  $\sim 3.8 \times 10^{13} \text{cm}^{-2}$  close to the protostar. The uncertainty varies across the map and has a mean value of  $\sim 3 \times 10^{12} \text{cm}^{-2}$ .

The uncertainties of the column density estimation are dominated by the assumptions of spectrum fitting. First, the largest error source for the derived column density is the uncertainty of the excitation temperature  $T_{ex}$ . Typically, the excitation temperature in dense cores and protostars is around 4-15K, depending on the source properties (e.g., Benson et al. 1998; Shirley et al. 2005; Kirk et al. 2007; Chen et al. 2007). In previous single-dish observations, the  $N_2H^+$  excitation temperature of L1157 was determined to be 8.9K by Emprechtinger et al. (2009), in general agreement with the rotational temperature of 13K obtained in Bachiller et al. (1993) using  $NH_3$  emission. In this study we assume a constant excitation temperature of 10K, and impose an uncertainty of 3K that is propagated with the other parameters. We used additional CARMA data that contain all hyperfine components in a lower spectral resolution for spectrum fitting with the CLASS package, and confirmed that the excitation temperature is around 10K near the protostar.

Second, we assume that the  $N_2H^+$  lines are optically thin. In fact, the average opacity from our spectrum fitting is 0.31, consistent with the assumption of optically thin. Nonetheless, the correction factor helps mitigate the errors propagated to column density. In addition, any self-absorption effect is neglected given the optically thin assumption. However, the optically thin approximation becomes worse toward the center, where  $\tau = 0.63 \pm 0.03$ .

LTE is assumed for the level populations of the rotational transitions. A constant proportionality between the hyperfine components is also adopted. The variation of the relative strengths between the hyperfine components as discussed in the appendix of Shirley et al. (2005) is ignored in this study.

For simplicity, we assume only one velocity component for the spectrum fitting, although this is not true in the inner envelope. We use a single Gaussian to fit the spectra over the map to estimate the  $N_2H^+$  column density. The simplification is insufficient for the more complex velocity structures near the center, but the resulting difference is smaller than the uncertainty caused by the excitation temperature assumption. For the kinematics of the envelope, see later sections for further discussion.

Unlike most  $N_2H^+$  studies, we fit the  $N_2H^+$  spectrum using only the isolated component instead of all seven sets of transitions. The 2MHz bandwidth in our observations cannot cover all seven sets simultaneously, so the excitation temperature distribution cannot be derived based on the relative strength between hyperfine components; therefore we assume a uniform excitation temperature. However, the difference should not be significant; it has been suggested that the two approaches

give results consistent within frequency resolution (e.g., Mardones et al. 1997; Emprechtinger et al. 2009).

Indeed, our derived  $\text{N}_2\text{H}^+$  column density of L1157 is comparable to other studies. For example, the column density was reported to be  $1.7 \times 10^{13} \text{cm}^{-2}$  in Bachiller & Perez Gutierrez (1997) and  $1.1 \times 10^{13} \text{cm}^{-2}$  in Emprechtinger et al. (2009), both using the IRAM 30m telescope with half-power beamwidth (HPBW) of  $27''$  with different assumptions of excitation temperature. Our average column density ( $1.0 \times 10^{13} \text{cm}^{-2}$ ) is slightly lower, as expected due to the interferometer resolving out large-scale emission.

#### 4.2. Correlation between $\text{N}_2\text{H}^+$ and $8 \mu\text{m}$ Absorption

The extended feature of  $\text{N}_2\text{H}^+$  emission coincides with the flattened absorption structure found in Looney et al. (2007). Figure 3 shows the absorption feature at  $8 \mu\text{m}$  overlaid with the contours of  $\text{N}_2\text{H}^+$  column density. At  $8 \mu\text{m}$ , the polycyclic aromatic hydrocarbon (PAH) emission provides a bright background, against which the dust extinction is detected. Note that the spatial resolution of *Spitzer* IRAC (the diffraction limit is  $1.8''$ ) is better than our  $\text{N}_2\text{H}^+$  observations (beam size is  $7.1'' \times 6.3''$ ). In general, the morphology of the absorbing dust is consistent with the  $\text{N}_2\text{H}^+$  gas, except the central region where the bipolar outflow feature dominates. From the  $8 \mu\text{m}$  map, the observed opacity is obtained given the assumption of a constant background estimated off-source. In Looney et al. (2007), a simple model of the flattened envelope was constructed; however, the power-law index of the density profile could not be constrained.

The observed opacities were converted into total column density and mass in Looney et al. (2007) with the assumption of a mass absorption coefficient of dust plus gas  $\kappa_{8.0\mu\text{m}} = 5.912 \text{cm}^2 \text{g}^{-1}$  from Li & Draine (2001). The total absorbing mass was estimated to be  $0.19 M_\odot$  in Looney et al. (2007). For a comparison, the mass of the same extended region is  $\sim 0.76 M_\odot$  based on the derived  $\text{N}_2\text{H}^+$  column density and a hypothetical constant  $\text{N}_2\text{H}^+$  abundance  $n(\text{N}_2\text{H}^+)/n(\text{H}_2)$  of  $3.0 \times 10^{-10}$ . Note that the central part of the flattened envelope is excluded here. Although most concentrated, the central region is dominated by the outflow activities at  $8 \mu\text{m}$ ; therefore the method of optical depth determination in Looney et al. (2007) is not applicable for regions within  $\sim 8.4''$  of the protostar. Also, the chemistry can become more complicated near the center so that the real  $\text{N}_2\text{H}^+$  distribution is not trivial. Furthermore, this comparison should not be overemphasized because of the following complexities: (1) an uncertain assumption of the  $\text{N}_2\text{H}^+$  abundance, (2) interferometric filtering, (3) the uncertainty of  $\kappa_{8.0\mu\text{m}}$ , and (4) ignorance of foreground emission when estimating mass using  $8 \mu\text{m}$  absorption (Tobin et al. 2009).

Nevertheless, the total column density, including gas and dust estimated from the  $8.0 \mu\text{m}$  extinction in Looney et al. (2007), can be compared with the  $\text{N}_2\text{H}^+$  column density derived from our spectrum fitting in this study. To facilitate the comparison for the flattened structure, we plot the profiles along the major axis of the flattened structure in Figure 4. Figure 4(a) shows the

$\text{N}_2\text{H}^+$  and estimated total column density, derived respectively from CARMA and *Spitzer* IRAC observations, for a cut of position angle  $75^\circ$  from north to east. The circles with error bars are the total column density from the absorption feature in Looney et al. (2007), and the thick curves with shades are the  $\text{N}_2\text{H}^+$  column density from this study.

As mentioned in the last section, the dominating uncertainty of the  $\text{N}_2\text{H}^+$  column density comes from the assumption of the excitation temperature  $T_{ex}$ . In our spectrum fitting, a constant  $T_{ex}$  of 10K is assumed. We estimate the uncertainty by imposing an uncertainty of excitation temperature  $\Delta T_{ex}=3\text{K}$  and the propagated error is shown as a color shaded region in Figure 4. Because the column density is monotonically increasing with  $T_{ex}$  (from Equations (1) and (3),  $\mathcal{N}_{tot} \propto Q(T_{ex})e^{\frac{E_1}{kT_{ex}}} \propto T_{ex}e^{\frac{E_1}{kT_{ex}}}$ ), the upper and lower bounds of the shaded region correspond to  $T_{ex}=13\text{K}$  and  $7\text{K}$ , respectively.

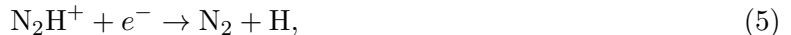
### 4.3. $\text{N}_2\text{H}^+$ Abundance

We estimate the  $\text{N}_2\text{H}^+$  abundance by taking the ratio of  $[\text{N}_2\text{H}^+]$ , from our CARMA observations, and  $[\text{H}_2]$ , derived in Looney et al. (2007), along a cut of the extended envelope. In Figure 4(b), the ratio of  $[\text{N}_2\text{H}^+]$  to  $[\text{H}_2]$  as a function of offset is plotted. Only the region away from the central outflow-dominating zone and with more than three S/N of  $\text{N}_2\text{H}^+$  detection is considered here. While the radial profile of the  $8\ \mu\text{m}$  absorption shows a good symmetry between east and west wings, the profile of  $\text{N}_2\text{H}^+$  does not. The  $\text{N}_2\text{H}^+$  column density drops in the west wing faster than the east. The average  $\text{N}_2\text{H}^+$  abundance is  $3.0 \times 10^{-10}$  in the east wing, lower than the average abundance  $5.7 \times 10^{-10}$  in the west wing. Our estimate of  $\text{N}_2\text{H}^+$  abundance is smaller than the value derived in Bachiller & Perez Gutierrez (1997,  $3.8 \times 10^{-9}$ ), while the difference can come from a different estimate of  $\text{H}_2$  column density and interferometric filtering. Nonetheless, the overall  $\text{N}_2\text{H}^+$  abundance is consistent with most chemical models. The typical  $\text{N}_2\text{H}^+$  abundance  $[\text{N}_2\text{H}^+]/[\text{H}_2]$  for prestellar cores and Class 0 YSOs varies from  $10^{-11}$  to  $10^{-9}$  (e.g., Aikawa et al. 2005; Maret et al. 2007; Tsamis et al. 2008), and likely changes with YSO evolution (e.g., Bergin & Langer 1997).

Enhancement of  $\text{N}_2\text{H}^+$  abundance close to the center is seen in the east wing (Figure 4(b)). This trend is also expected by chemical models. While the preceding objects, starless cores, have been shown to have constant  $\text{N}_2\text{H}^+$  abundance (Tafalla et al. 2002), the abundance profile evolves as a function of radius in the collapsing cores (e.g., the numerical chemical models: Lee et al. 2004; Aikawa et al. 2005; Tsamis et al. 2008). In particular, the formation and destruction of  $\text{N}_2\text{H}^+$  is closely related to other species by the chemical reactions with  $\text{N}_2$  and  $\text{CO}$  (Womack et al. 1992; Jørgensen et al. 2004). The dominant route to form  $\text{N}_2\text{H}^+$  is through



while it is destroyed by dissociative electron recombination at high temperature





and CO destroys  $\text{N}_2\text{H}^+$  in the gas phase by the reaction



Therefore, when CO starts to deplete onto dust grains at densities around  $2\text{--}6 \times 10^4 \text{ cm}^{-3}$  (e.g., Tafalla et al. 2002) in the inner envelope, the abundance of  $\text{N}_2\text{H}^+$ , as well as other nitrogen-bearing molecules, increases.

On the other hand, depletion of  $\text{N}_2\text{H}^+$  is also expected in the inner envelope. The depletion density is around  $10^6 \text{ cm}^{-3}$  to  $3 \times 10^7 \text{ cm}^{-3}$ , above which the gaseous  $\text{N}_2\text{H}^+$  start to deplete (Bergin & Langer 1997; Aikawa et al. 2003). However, whether depletion is seen in our observations is not clear due to the fact that the region with density higher than the depletion density is not well resolved with the observational beam size. Also, information of extinction and total column density is missed owing to the bright outflow activity at  $8 \mu\text{m}$ , making us unable to obtain the  $\text{N}_2\text{H}^+$  abundance near the center. Furthermore, the CO molecules, existing in the outflows or evaporated from the dust grains in the very inner envelope due to the heating from the central protostar, can destroy the  $\text{N}_2\text{H}^+$  molecules (Lee et al. 2004); the CO outflow and evaporation effects can look similar to the depletion effect from the observational point of view. Eventually, a more careful study for L1157, such as Evans et al. (2005) for B335, a similar protostar at the same evolutionary stage as L1157, will be needed to consider multiple species and understand the system more thoroughly.

#### 4.4. Simple Dust Modeling

While a large scale flattened envelope is detected by  $\text{N}_2\text{H}^+$  emission, the dust emission at 3 mm is compact and round; the goal in this section is to construct a model that can interpret both. To do so, we begin with fitting the dust continuum. We constructed a model that has a flattened geometry similar to the  $\text{N}_2\text{H}^+$  feature and predicts an observed spherical dust continuum.

We have developed a radiative transfer code that considers density and temperature structures in three dimensions to do the dust continuum modeling, and compare with visibilities from interferometric observations. First, a map of flux density is obtained with high numerical resolution given a model envelope. For each pixel on the plane of sky, the flux is calculated by integrating the dust emission along the line of sight (e.g., Adams 1991). The specific intensity can be expressed as

$$I_\nu = \int_{los} B_\nu(T) e^{-\tau_\nu} d\tau_\nu = \int_{los} B_\nu(T(\vec{r})) e^{-\tau_\nu(\vec{r})} \rho(\vec{r}) \kappa_\nu d\vec{r}, \quad (7)$$

where  $B_\nu(T)$  is the Planck function at dust temperature  $T$ ,  $\tau_\nu$  is the optical depth from the position  $\vec{r}$  along the line of sight to the observer,  $\rho$  is the envelope density, and  $\vec{r}$  denotes the position.  $T$ ,  $\rho$ , and  $\tau_\nu$  are all functions of  $\vec{r}$ . In this study, the opacity of dust grains  $\kappa_\nu$  is assumed to be uniform throughout the envelope. We simulated all observational effects from the interferometric observations. The image is corrected by the primary beam effect according to the antenna size, and

Fourier transformed into visibilities with the observational  $u$ - $v$  sampling. In the case of CARMA, the 6m BIMA dishes and 10m OVRO dishes give three different primary beams. Therefore we constructed separate primary-beam-corrected images for each kind of baseline, and sampled them with corresponding  $u$ - $v$  spacings from real observations. However, the mosaic pattern was not considered in the dust modeling, although a five-pointing mosaic was used in the observations. The dust continuum is very compact with size much smaller than the FWHM of the primary beam, hence the effect is insignificant. Finally, the modeled visibilities are binned into  $u$ - $v$  annuli around the source center and averaged vectorially. The flux density for each bin is compared with the observations, which are binned in the same way using the MIRIAD task UVAMP, as shown in Figure 5 by crosses with error bars. A  $\chi_r^2$  value is calculated to quantify the goodness of a fit. The comparison is done in visibility space so uncertainty from imaging processes such as the CLEAN algorithm is avoided.

The code has been tested for accuracy and convergency. The results of spherically symmetric cases were checked by comparing with those obtained by previous codes used in Looney et al. (2003) and Chiang et al. (2008). Because of the nature of higher density and higher derivatives in the inner envelope, smaller step sizes are required for the inner region. On the other hand, step size is not as sensitive for the outer region, so computing time is saved by using coarser steps. In the current code, three refinements of step sizes are used with extra fine steps taken for the very central region to achieve accuracy better than observational uncertainties. Also, cases of different numerical resolutions have been run to check convergency. In this study, the numerical resolution is 37.5AU, corresponding to 0.15'' for L1157. Higher numerical resolution gives consistent flux density within a difference smaller than 0.05 mJy. In addition, the code itself does not assume any symmetry. In other words, the model of envelope density and temperature can be arbitrary in three dimensions.

With the observed flattened structure in mind, we construct a model envelope of similar morphology. For simplicity, we adopted a power-law density and temperature profile. To impose the flattened geometry, we use a spherically symmetric distribution and taper the density profile with a Gaussian mask diminishing along the minor axis of the disk orientation. In our model, the vertical scale height of the Gaussian is fixed to be 2000 AU for an ellipticity close to the observed flattened feature. We orientate the flattened envelope as the observed  $\text{N}_2\text{H}^+$  feature, that is, with a position angle of  $75^\circ$ . We also adopt an inclination angle of  $80^\circ$ , as determined from outflow observations (Gueth et al. 1996). However, the temperature distribution remains spherically symmetric.

Note that this model is not physically motivated, but it interprets the observations with statistical significance. We adopt a power-law index of -2 for the density structure, similar to a singular isothermal sphere in the extreme case of a Bonnor-Ebert sphere (Shu 1977). The dust temperature profile is a power law of index  $-2/(4+\beta)$ , where  $\beta$  is the spectral index of opacity, from the spherically symmetric approximation assuming the heating is dominated by the central source (Adams 1991). We set the extrapolated temperature at 1AU to be 300K and a lower limit of 5K representing

the external heating from cosmic ray or interstellar radiation.

For the dust grain properties, a fiducial value of the mass opacity coefficient  $\kappa_{3mm}=0.0056 \text{ cm}^2\text{g}^{-1}$  is adopted, based on  $\kappa_{1mm}=0.01 \text{ cm}^2\text{g}^{-1}$  (e.g., Natta et al. 2004) and  $\beta = 0.5$  (Kwon et al. 2009). The exact value of  $\kappa$  is uncertain and can vary by an order of magnitude dependent on the grain properties (e.g., the interstellar MRN grains in Draine & Lee 1984 and the coagulated grains in Ossenkopf & Henning 1994). Nevertheless,  $\kappa_\nu$  is expected to follow a power law with frequency  $\nu$  at long wavelengths, that is,  $\kappa \propto \nu^\beta$ . The extrapolation at millimeter wavelengths is determined by the spectral index  $\beta$ , which is dependent on grain size, grain geometry, chemical composition, etc (Draine 2006). For a young object like L1157, grain growth may have already started in the inner region. For simplicity, the dust grain properties is assumed to be uniform across the envelope and not dependent on the radius. The possible radial gradient of grain properties, which was recently reported by Kwon et al. (2009), is neglected in this study.

We have explored two parameters: point-source flux ( $F_p$ ), representing the flux contribution from the embedded circumstellar disk system inside the inner radius of the model envelope, and the extrapolated density at 1AU ( $d_1$ ), scaling with the total mass. A grid of model parameters is run with  $F_p$  from 0 to 30 mJy in steps of 1 mJy, and  $d_1$  from  $4 \times 10^{-12}$  to  $20 \times 10^{-12} \text{ g cm}^{-3}$  in steps of  $0.5 \times 10^{-12} \text{ g cm}^{-3}$ . The inner and outer radius of the envelope are fixed to be 5AU and 15,000AU, respectively. Varying the outer radius of the envelope does not make a big difference because little flux is emitted from the low-density region compared to the denser region. Also, the interferometer resolves out some of the large-scale emission. The inner radius is correlated to the point-source flux and can be chosen as long as it is much smaller than the observational spatial resolution, while physically the dust destruction radius is of the order of 0.1AU, inside which the temperature is too high for dust to exist. A summary of the  $\chi_r^2$  model fitting is shown in Figure 6. The filled circle marks the best fit and the contours show the parameter ranges with different confidence levels. The two parameters are correlated and cannot be clearly distinguished, because either a big density scaling factor  $d_1$  or a high point-source flux  $F_p$  can result in a high peak of flux density. The best-fit model has a point-source flux  $F_p = 1 \text{ mJy}$  and extrapolated density at 1AU  $d_1 = 1.35 \times 10^{-11} \text{ g cm}^{-3}$ . A total envelope mass of  $1.5 M_\odot$  is then implied in our model; this mass is generally consistent with other mass estimates (e.g., Shirley et al. 2000; Gueth et al. 2003; Froebrich 2005). The modeled flux density of the best fits as a function of  $uv$  distance is shown by the curve in Figure 5.

We estimate the corresponding  $\text{N}_2\text{H}^+$  column density of the best-fit model obtained from the dust continuum fitting. To do the conversion, the dust-to-gas ratio is assumed to be uniformly 1/100, as the typical value in the interstellar medium, and the  $\text{N}_2\text{H}^+$  abundance is assumed to be uniformly  $3.0 \times 10^{-10}$ . Further, we simulate the depletion effect by introducing a threshold depletion density, above which the  $\text{N}_2\text{H}^+$  density does not increase with  $\text{H}_2$  density. We adopt a depletion density of  $1.5 \times 10^6 \text{ cm}^{-3}$ . To compare with observations,  $\text{N}_2\text{H}^+$  volume density is integrated along the line of sight to calculate the column density across the map. The model  $\text{N}_2\text{H}^+$  column density and the detected  $\text{N}_2\text{H}^+$  emission are shown in Figure 7.

As seen in Figure 7, our best-fit dust model gives a consistent map of  $\text{N}_2\text{H}^+$  column density. This simple model illustrates how we do not observe extended dust continuum while the  $\text{N}_2\text{H}^+$  emission is detected to be extended more than  $80''$  across. The dust emission, which depends on both density and temperature, in the outer region of the flattened envelope is too weak to be detectable by these observations.

## 4.5. Gas Kinematics

The complex  $\text{N}_2\text{H}^+$  spectral information reveals a composite system of multiple dynamic components (Figure 3(b)). To understand the detailed kinematics, we perform a simple analysis using position-velocity (PV) diagrams. Figure 8(b) shows the PV diagram for the  $\text{N}_2\text{H}^+$   $JF_1F=101-012$  component along the major axis of the flattened envelope at position angle  $75^\circ$  from north to east. This transition is isolated so no confusion is caused due to blending with other hyperfine lines.

We construct a simple model to simulate the PV diagram assuming various velocity structures of the envelope. Note that the kinematics modeling is independent of the dust modeling, except that the best-fit density structure from the previous section is used. We adopt the procedure as discussed in Ohashi et al. (1997a) and consider a spatially thin cut along the major axis of the envelope. Both the inclination and opacity effects are ignored. The column density in each velocity channel as a function of offset is estimated by integrating density along the line of sight and sorting into observational spectral bins by the projected velocity. The depletion effect is simulated by assuming constant  $\text{N}_2\text{H}^+$  density for the central region where  $\text{H}_2$  gas density is higher than  $1.5 \times 10^6 \text{cm}^{-3}$ , the same depletion density as adopted in the previous section. With the depletion effect, the actual density structure of the inner envelope does not play a large role. The spatial distribution is then convolved with the observational beam. However, unlike the dust modeling, the interferometric filtering effects are not taken into account for the kinematics study. Nonetheless the large-scale emission from background clouds is not included; this is similar to interferometry resolving out large scale emission. Finally, the modeled results are shown by contours in PV diagrams and compared with observations.

### 4.5.1. Spectroscopic Signatures of Infall Motion

The double-peaked feature seen in the central region indicates multiple velocity components in the protostellar envelope (Figure 8(a)). The redshifted and blueshifted peaks have a velocity difference of  $\sim 0.4 \text{ km s}^{-1}$ , inferring a relative motion between two parts of the envelope. One interpretation for this is the infall motion of the inner envelope, which can also be the cause of the high-velocity wings. Gravitational collapse takes place in the early stage of star formation (e.g., theoretical studies in Shu 1977; Hunter 1977; Tassis & Mouschovias 2005). However, the predicted infall velocity structures are very different from model to model, especially in the inner

envelope. Detailed comparison of various theoretical models with observations is beyond the scope of this paper and may be studied with observations of higher spatial and spectral resolutions in the future. Nevertheless, infall is expected in the inner envelope of L1157. Previously, L1157 has been identified as an infall candidate by single dish (Gegersen et al. 1997; Mardones et al. 1997) and interferometric observations (Gueth et al. 1997; Beltrán et al. 2004). In addition, detection of methanol from the accretion shocks on the small scale also supports the picture of envelope material infalling onto the forming protostellar disk (Velusamy et al. 2002).

Figure 9(a) shows the modeled PV contours for a pure infall motion. A simple velocity profile  $v \sim r^{-1/2}$ , representing ideal free-fall, is used. The simple infall model shows a double-peaked feature toward the center of the envelope, as obtained by Ohashi et al. (1997a). However, the model cannot explain the asymmetry of the peaks. A more sophisticated model that considers full geometry, radiative transfer, and different theoretical profiles such as Momose et al. (1998) may be necessary.

We exclude this double-peaked feature as arising from self-absorption, commonly used as an indicator of infall motion in the prestellar cores (e.g., Evans 1999). In such an approach of identifying infall candidates, a stronger blueshifted peak and a weaker redshifted peak are expected for infalling sources observed by an opaque line because the front half of the cloud causes a redshifted absorption dip (e.g., Myers et al. 1996; Masunaga & Inutsuka 2000), while an optically thin line should be observed within two velocity peaks. In this specific case, since the  $N_2H^+$  lines are moderately optically thin, this scenario of self-absorption is ruled out, although a similar profile is observed. However, the spectrum is sensitive to the detailed envelope model such as optical depth, turbulent velocity dispersion, spatial structures of velocity, density, and excitation temperature, etc (e.g., Zhou 1992; Ward-Thompson & Buckley 2001). The complexity makes it difficult to justify the real physical properties causing the observed spectra. In addition, the interferometry selectively observes the small-scale emission, leaving out the large-scale static cloud in the outer envelope and resulting in spectrum with a deeper zero-velocity dip (Choi 2002).

While a double peaked profile of  $N_2H^+$  is seen in our interferometric observations, Mardones et al. (1997) observed the same line using IRAM 30m telescope, and found it to be single-peaked and used it as the optically thin reference to compare with other optically thick lines for studying infall. The same source was observed again by the IRAM 30m telescope in Emprechtinger et al. (2009) and similar results were obtained. <sup>6</sup> These support our spectrum fitting results that the  $N_2H^+$  J=1-0 lines are optically thin. The major differences of our observation are a smaller beam size and the aperture synthesis. Therefore the cause of discrepancy is deduced to be (1) a beam-smearing effect and/or (2) interferometric filtering. While the overall spectrum is dominated by the inner envelope, the small-scale structures are not distinguishable by the single-dish observations. However, observations of higher resolutions with interferometers reveal other complexities. For example, the

---

<sup>6</sup>However, our recent spectral data taken by IRAM 30m seems to show a double-peaked feature in the strongest hyperfine component (J.J. Tobin et al. in preparation). More careful examination is in process.

degree of profile asymmetry can be enhanced if observed with a higher angular resolution (Choi 2002). Also, we test our modeling routine by convolving the spectrum with different beam sizes, and confirm the beam-smearing effect. A double-peaked feature can look like a single Gaussian if the observational beam size is not able to resolve the infall radius.

Second and more importantly, interferometric observations reveal only the targeted protostellar envelope at the expense of missing flux from large-scale structures, arguably dominated by the static foreground and background clouds. Choi (2002) has shown that missing short spacing flux can affect the self-absorption dip for optically thick lines. It can cause similar effects for optically thin lines too. In particular, large scale background material is mostly static compared to the infalling inner envelope and contributes more flux at the LSR velocity. Nonetheless, the material in the large scale cloud does not participate in star formation as actively as the inner envelope. For comparison with the spectrum of IRAM 30m single-dish observations (Mardones et al. 1997; Bachiller & Perez Gutierrez 1997; Emprechtinger et al. 2009), we smooth our images with a  $27''$  Gaussian beam (the beam size of IRAM 30m observations) and found that  $\sim 20\%$  of the total flux is filtered out by CARMA, also causing a dip around the LSR velocity.

A large line width of  $\text{N}_2\text{H}^+$   $J=1-0$  is found by the single dish observations. The fitted line widths of the single-peaked spectra are  $0.71$  and  $0.65$   $\text{km s}^{-1}$  for the IRAM 30m observations in Mardones et al. (1997) and Emprechtinger et al. (2009), respectively. We compare the single-dish observations with our smoothed spectrum. If we fit our double-peaked spectrum with a single Gaussian, the FWHM is  $0.88 \pm 0.05$   $\text{km s}^{-1}$ . But if we fit the spectrum with two Gaussians of the same width, the FWHM is  $0.44 \pm 0.02$   $\text{km s}^{-1}$ , comparable to the sonic line width  $\sim 0.45$   $\text{km s}^{-1}$  and larger than the thermal line width  $\sim 0.13$   $\text{km s}^{-1}$  with the assumed temperature of 10K. The dynamics at small scales can be obscured in single-dish observations but can be revealed by high-resolution interferometric observations. If this phenomenon is common to other sources, it may be why the average line width of Class 0 YSOs is large ( $\sim 0.61$   $\text{km s}^{-1}$ , Emprechtinger et al. 2009) compared to that of starless cores ( $0.2-0.4$   $\text{km s}^{-1}$ , Lee et al. 2001).

We cannot exclude the possibility that the double-peaked feature is caused by factors other than infall motion in the inner envelope. For example, outflows contaminate the molecular tracers of envelope material. A similar case of the Class 0 protostar B335 was studied by Wilner et al. (2000). While the single-dish observation matched well with the inside-out infall model (Zhou et al. 1993), the interferometric observation brought up a more realistic scenario. The optically thin CS  $J=5-4$  line is shown to be dominated by small-scale outflow clumps in high-resolution observations (Wilner et al. 2000). A single-peaked spectrum seen in low-resolution observations can contain two velocity components and hence a double-peaked feature is shown with interferometric filtering. However, some molecular lines do not trace outflows as closely as other species. It has been suggested that  $\text{N}_2\text{H}^+$  lines trace the quiescent cores but not the shocked outflow gas (Bachiller 1996). The CO molecules in the outflows can destroy the  $\text{N}_2\text{H}^+$  molecules (Equation (6)). Indeed, while the abundance of some species is enhanced by the outflow shocks,  $\text{N}_2\text{H}^+$  is not detected at the shock regions (Bachiller & Perez Gutierrez 1997). In other words, the outflow contamination

is minimized for this specie, although some outflow effects are unavoidable (for example, see the outflow-envelope interface at the southeast extension in Figure 1(b)).

The double-peaked spectrum can also be caused by unrelated dense clumps that happen to be in the same line of sight. This is less likely because channel maps do not show traits of unrelated components. If clumps exist in the foreground or background, they are more likely to show up individually at a peculiar velocity. In contrast, the morphology of the envelope at different velocities are systematically consistent in our observations. Also,  $\text{N}_2\text{H}^+$  does not pick up other velocity components as easily as CO because it requires high densities to form. Infall motion, not necessarily gravitational infall, is suggested.

#### 4.5.2. Rotation

While axisymmetric infall cannot explain the velocity difference between the east and west extensions of the envelope, the differential velocity may come from rotation of the envelope. In this section, we test some simple rotation curves.

First, we test Keplerian rotation. If the dynamics of the envelope is dominated by Keplerian rotation around a central point mass much larger than the cumulative envelope mass, the central mass has to be smaller than  $0.1 M_\odot$  to explain the observed velocity differential of the envelope. In Figure 9(b), the pure Keplerian curves for a point mass of 0.01, 0.02, and 0.04 are shown. Apparently, the deduced central mass is around or even smaller than the mass of the envelope, which means that the cumulative envelope mass cannot be neglected. This is expected because for Class 0 YSOs, mass is mostly distributed in the envelope rather than the central protostar (e.g., Andre et al. 1993). Next, we consider complete Keplerian rotation with cumulative envelope mass. The velocity is  $(GM_R/R)^{1/2}$ , where  $M_R$  is the mass contained within the radius  $R$ . An envelope with  $\rho \propto r^{-2}$  gives a flat rotation curve. The best-fit density obtained in the previous dust continuum fitting gives a roughly constant rotation velocity  $0.5 \text{ km s}^{-1}$ , much larger than the observed value. These exercises show that Keplerian rotation is ruled out for the large-scale envelope.

In fact, the system is too young to construct large-scale Keplerian rotation. For example, the period of rotation with velocity  $0.2 \text{ km/s}$  at  $1000 \text{ AU}$  is  $\sim 1.5 \times 10^5 \text{ yr}$ , larger than the typical age of Class 0 protostars. As seen in the PV diagram, the size scale of rotation is around  $10,000 \text{ AU}$  and requires even longer dynamical timescale. Again, the dynamical time estimation suggests the unsuitability of pure Keplerian rotation for this system.

Another possible scenario is that there exists solid-body rotation in L1157. This has been seen in other Class 0 YSOs such as HH212 (Wiseman et al. 2001). The solid-body rotation is probably inherited from the initial conditions of the large-scale clouds or filaments. Angular momentum plays an important role in the protostar evolution (e.g., Bodenheimer 1995). In particular, the initial condition of rotation is closely related to the core morphology and fragmentation (e.g., Saigo et al. 2008). The extended envelope of L1157 has a velocity gradient of around  $1.5 \text{ km s}^{-1} \text{ pc}^{-1}$  assuming

solid-body rotation (shown by the dashed line in Figure 9(b) and (c)). The velocity gradient is much smaller than what was found in the survey of Class 0 protostars ( $\sim 7 \text{ km s}^{-1} \text{ pc}^{-1}$ , Chen et al. 2007); instead, it resembles the typical velocity gradient found in the dense clouds ( $1\text{-}2 \text{ km s}^{-1} \text{ pc}^{-1}$ , Goodman et al. 1993; Caselli et al. 2002). Moreover, the rotating  $\text{N}_2\text{H}^+$  envelope of L1157 has a size scale much larger than the typical size scale of collapsing envelopes. Both the large size and the slow bulk rotation imply properties more similar to prestellar cores than collapsing envelopes. After the protostar has formed in the central densest region, the kinematics of the envelope can still be dominated by the remnant rotation of the parent dense cloud at large scales, while the infall motion takes over at small scales. The good alignment of the rotation with other features such as flattened geometry and outflow direction also suggest a consistent picture.

Considering the envelope with radius of 10,000AU and the fitted solid-body rotation, the specific angular momentum is around  $4 \times 10^{-3} \text{ km s}^{-1} \text{ pc}$ . We can locate it at a specific angular momentum–rotation radius plot to compare with the other dense cores and protostars (e.g., Ohashi et al. 1997b; Belloche et al. 2002; Chen et al. 2007). Although as an infalling envelope at small scales, the large-scale properties of the L1157 flattened envelope resemble those of prestellar cores more than those of more evolved protostars. Additionally, the fitted angular velocity implies that if the large-scale envelope collapses to form a circumstellar disk, the envelope material would fall onto the midplane within a centrifugal radius of  $r_c = R^4 \Omega^2 / GM \approx 500 \text{ AU}$ . This radius is much larger than the observed T Tauri disks. All above implies that the large-scale flattened envelope is probably not involved in the dynamical infall activity.

The interpretation of solid-body rotation is well suited from many theoretical points of view. For example, magnetic braking can induce solid-body rotation (Basu & Mouschovias 1994). A turbulent core can also yield velocity gradient similar to uniform rotation (Burkert & Bodenheimer 2000). Here we calculated the  $\beta_{rot}$  parameter, defined as the ratio of rotational kinetic energy to gravitational energy  $\beta_{rot} = \frac{\frac{1}{2} I \Omega^2}{qGM^2/R} = \frac{p\Omega^2 R^3}{2qGM}$ , at different radii of the flattened envelope. (Note that this  $\beta_{rot}$  is different from the opacity spectral index mentioned in the previous sections.) For L1157,  $\beta_{rot}$  is smaller than 2% throughout the envelope, suggesting that the flattened structure is not supported by rotation.

The combined best-fit model of simple infall and solid-body rotation is shown by the black contours in Figure 9(c). Both the double-peaked feature and the large-scale velocity gradient can be explained by this model. However, the asymmetric features are impossible to model with an axisymmetric model in the optically thin case. Local clumpiness can be the cause of asymmetry. Without further observations with higher spatial and spectral resolutions it is hard to justify the detailed properties.



#### 4.6. Overall Gas-Dust Comparison and Global Picture of L1157

By considering the dust and gas information of Class 0 YSO L1157 altogether, we are able to construct an overall physical picture of the system. The dust absorption at  $8\ \mu\text{m}$  from *Spitzer* shows a large-scale extended dense cloud that is flattened perpendicular to the outflow direction, while the 3 mm dust emission from CARMA D- and E-array shows a compact spherical structure. These two observations of dust detect different components of the envelope. The extended envelope detected by  $8\ \mu\text{m}$  absorption is likely part of the parent cloud, while the very inner region seen by our dust continuum is the collapsing envelope. The flattened geometry may result from physical processes of core formation. On the other hand, the  $\text{N}_2\text{H}^+$  emission provides a consistent view both morphologically and kinematically. The  $\text{N}_2\text{H}^+$  feature coincides with the extended dust absorption seen at  $8\ \mu\text{m}$ , meaning that the same cloud component is observed. A slow solid-body rotation at large scales is seen along the major axis of elongation, but the flattened structure is not supported by rotation. This parent cloud resembles the physical properties of a prestellar core, while the innermost region is decoupled and undergoes (gravitational) collapse.

A similar dynamical scenario has also been suggested for another Class 0 object, IRAM 04191+1522 (Belloche et al. 2002). They have obtained a decoupling radius of  $\sim 3500\text{AU}$ , which divides the envelope into a rapidly rotating inner region with free-fall motion and a transition region connected to the ambient slowly rotating cloud. Their estimated angular velocity at large scales ( $\sim 1.9\ \text{km s}^{-1}\ \text{pc}^{-1}$  at 7000 AU and  $\lesssim 0.5\text{-}1\ \text{km s}^{-1}\ \text{pc}^{-1}$  at 11,000 AU) are comparable to what we find for L1157. More recent interferometric observations revealed faster rotation at smaller scales, but resolved out the large-scale structures (Belloche & André 2004; Lee et al. 2005).

We construct an edge-on disk-like envelope model that fits our L1157 data. Given the estimated column density and assumptions of envelope geometry, the volume density averaged along the line of sight can be estimated. With the assumption of an outer radius of 15,000AU and a constant  $\text{N}_2\text{H}^+$  abundance of  $3.0 \times 10^{-10}$ , as used in our dust modeling, the average gas volume density ranges from  $\sim 2 \times 10^4$  to  $\sim 3 \times 10^5\ \text{cm}^{-3}$ . This volume density is consistent with the detectable density of  $\text{N}_2\text{H}^+$ , that is, it is close to the critical density  $10^5\ \text{cm}^{-3}$ . On the other hand, the average density should not be higher than the depletion density ( $\sim 10^6\text{-}10^7\ \text{cm}^{-3}$ ); this can give a constraint on the thickness of the cloud.

The geometric structures of L1157 at different size scales are shown at various observations (Figure 10). At small scales, L1157 shows a nearly spherical morphology, as commonly seen in other YSOs (e.g., Looney et al. 2000; Shirley et al. 2000); detailed comparisons between observations and theories of collapsing envelopes are usually done assuming spherical symmetry (e.g., Looney et al. 2003). In particular, high-resolution observations done by interferometry only show the contributions from the inner envelope while the large-scale structures are mostly resolved out. Deviation from spherical symmetry can be significant, especially at large scales. At a younger stage of evolution, large-scale dense cores are commonly observed to be elongated (e.g., Myers et al. 1991). Although the underlying dynamical processes of the flattened cores are controversial (e.g.,

Gammie et al. 2003; Tassis 2007; Offner & Krumholz 2009), non-spherical structure in the initial condition can play an important role for their evolution (e.g., Galli & Shu 1993; Hartmann et al. 1996). For L1157, both the  $\text{N}_2\text{H}^+$  feature and  $8\ \mu\text{m}$  absorption reveal the flattened structure at the size scale of  $\sim 0.1$  pc, comparable to a typical prestellar core. At a larger scale, the morphology becomes even more irregular. For example, the Digitized Sky Survey (DSS)<sup>7</sup> optical image of L1157 shows a large-scale structure of irregular shape. This is more like the initial condition but not the consequence of star formation. The cloud is filament-like and irregular at very large scale, while a nearly spherical inner envelope is embedded in the intermediate-size, flattened outer envelope extended perpendicular to the outflows.

L1157 is an interesting and relatively simple case for early star formation. While many Class 0 YSOs are associated with large-scale non-axisymmetric outer envelopes, the geometry of L1157 is highly flattened and symmetric (Tobin et al. 2009). L1157 is a perfect site for observational experiments, presenting a typical Class 0 YSO with less complexity. The properties of L1157 may be generalized to other Class 0 YSOs. For example, the Class 0 collapsing envelope with its embedded protostar is surrounded by the outer envelope left by its parent core that may or may not gravitationally collapse at a later time. In the case of L1157, we are able to detect this outer envelope in a flattened structure at both  $8\ \mu\text{m}$  and  $\text{N}_2\text{H}^+$  emission, revealing a phase that shows both properties of the preceding prestellar core stage at large scale and properties of the current Class 0 stage at small scale. In other cases, the outer envelope can become more complicated that a non-axisymmetric model will be needed to interpret the observations.

## 5. Summary

1. We observed the dust continuum and  $\text{N}_2\text{H}^+$  gas emission at 3 mm toward the Class 0 YSO L1157 IRS with an angular resolution of  $\sim 7''$  using CARMA at D- and E-array. Spectra of the  $\text{N}_2\text{H}^+$  isolated component  $JF_1F=101-012$  were obtained with resolution of  $\sim 0.1\ \text{km s}^{-1}$ . While the 3 mm dust continuum detects the inner envelope, which is compact and nearly spherical, the  $\text{N}_2\text{H}^+$  emission shows a huge flattened structure with a linear size of  $\sim 20,000\text{AU}$ , coinciding with the disk-like feature found by the  $8\ \mu\text{m}$  absorption in Looney et al. (2007).
2. By fitting the spectra, we estimated the gas column density across the flattened envelope and compared with the dust column density deduced from the  $8\ \mu\text{m}$  absorption feature. We derived the  $\text{N}_2\text{H}^+$  abundance and found results consistent with what is expected from chemical models. Further, we examined the radial profile of  $\text{N}_2\text{H}^+$  abundance along the major axis of the flattened envelope, and showed the asymmetry between the east and west extension.

---

<sup>7</sup>The Digitized Sky Survey was produced at the Space Telescope Science Institute under U.S. Government grant NAG W-2166. The images of these surveys are based on photographic data obtained using the Oschin Schmidt Telescope on Palomar Mountain and the UK Schmidt Telescope. The plates were processed into the present compressed digital form with the permission of these institutions.

3. We constructed a simple flattened envelope model that fits the compact dust continuum; further, the model-expected gas column density is consistent with the extended  $\text{N}_2\text{H}^+$  emission. It follows that the deviation from spherical symmetry can be important at large scales for protostellar envelopes. However, this model is not motivated by a theoretical model.
4. We did PV contour modeling and studied the kinematics of the  $\text{N}_2\text{H}^+$  feature. The spectrum of the central part of the system shows a double-peaked feature, implying infall. The large-scale component can be described by slow solid-body rotation comparable to the properties of a typical prestellar core. This large-scale filament may arguably result from the dynamical processes in the early core formation, while only the very inner part is actively involved in the protostar formation.

H.-F. C. is grateful to C. F. Gammie for insightful discussions and comments. We thank the anonymous referee for the valuable comments. H.-F. C. and L. W. L. acknowledge support from the Laboratory for Astronomical Imaging at the University of Illinois and the NSF under grant AST-07-09206 and NASA Origins grant NNG06GE41G. We thank the OVRO/CARMA staff and the CARMA observers for their assistance in obtaining the data. Support for CARMA construction was derived from the states of Illinois, California, and Maryland, the Gordon and Betty Moore Foundation, the Eileen and Kenneth Norris Foundation, the Caltech Associates, and the National Science Foundation. Ongoing CARMA development and operations are supported by the National Science Foundation under cooperative agreement AST-0540459, and by the CARMA partner universities.

## REFERENCES

- Adams, F. C. 1991, *ApJ*, 382, 544
- Aikawa, Y., Herbst, E., Roberts, H., & Caselli, P. 2005, *ApJ*, 620, 330
- Aikawa, Y., Ohashi, N., & Herbst, E. 2003, *ApJ*, 593, 906
- Andre, P., Ward-Thompson, D., & Barsony, M. 1993, *ApJ*, 406, 122
- . 2000, *Protostars and Planets IV*, 59
- Arce, H. G., Santiago-García, J., Jørgensen, J. K., Tafalla, M., & Bachiller, R. 2008, *ApJ*, 681, L21
- Bachiller, R. 1996, *ARA&A*, 34, 111
- Bachiller, R., Martin-Pintado, J., & Fuente, A. 1993, *ApJ*, 417, L45
- Bachiller, R., & Perez Gutierrez, M. 1997, *ApJ*, 487, L93

- Bachiller, R., Pérez Gutiérrez, M., Kumar, M. S. N., & Tafalla, M. 2001, *A&A*, 372, 899
- Basu, S., & Mouschovias, T. C. 1994, *ApJ*, 432, 720
- Belloche, A., & André, P. 2004, *A&A*, 419, L35
- Belloche, A., André, P., Despois, D., & Blinder, S. 2002, *A&A*, 393, 927
- Beltrán, M. T., Gueth, F., Guilloteau, S., & Dutrey, A. 2004, *A&A*, 416, 631
- Benson, P. J., Caselli, P., & Myers, P. C. 1998, *ApJ*, 506, 743
- Bergin, E. A., & Langer, W. D. 1997, *ApJ*, 486, 316
- Bock, D., et al. 2006, in *Society of Photo-Optical Instrumentation Engineers (SPIE) Conference Series*, Vol. 6267
- Bodenheimer, P. 1995, *ARA&A*, 33, 199
- Burkert, A., & Bodenheimer, P. 2000, *ApJ*, 543, 822
- Caselli, P., Benson, P. J., Myers, P. C., & Tafalla, M. 2002, *ApJ*, 572, 238
- Caselli, P., Myers, P. C., & Thaddeus, P. 1995, *ApJ*, 455, L77
- Chen, X., Launhardt, R., Bourke, T. L., Henning, T., & Barnes, P. J. 2008, *ApJ*, 683, 862
- Chen, X., Launhardt, R., & Henning, T. 2007, *ApJ*, 669, 1058
- Chiang, H.-F., Looney, L. W., Tassis, K., Mundy, L. G., & Mouschovias, T. C. 2008, *ApJ*, 680, 474
- Choi, M. 2002, *ApJ*, 575, 900
- Daniel, F., Cernicharo, J., & Dubernet, M.-L. 2006, *ApJ*, 648, 461
- Draine, B. T. 2006, *ApJ*, 636, 1114
- Draine, B. T., & Lee, H. M. 1984, *ApJ*, 285, 89
- Emprechtinger, M., Caselli, P., Volgenau, N. H., Stutzki, J., & Wiedner, M. C. 2009, *A&A*, 493, 89
- Evans, N. J., et al. 2009, *ApJS*, 181, 321
- Evans, II, N. J. 1999, *ARA&A*, 37, 311
- Evans, II, N. J., Lee, J.-E., Rawlings, J. M. C., & Choi, M. 2005, *ApJ*, 626, 919
- Froebrich, D. 2005, *ApJS*, 156, 169

- Galli, D., & Shu, F. H. 1993, *ApJ*, 417, 220
- Gammie, C. F., Lin, Y.-T., Stone, J. M., & Ostriker, E. C. 2003, *ApJ*, 592, 203
- Goldsmith, P. F., & Langer, W. D. 1999, *ApJ*, 517, 209
- Goldsmith, P. F., Langer, W. D., & Velusamy, T. 1999, *ApJ*, 519, L173
- Goodman, A. A., Benson, P. J., Fuller, G. A., & Myers, P. C. 1993, *ApJ*, 406, 528
- Green, S., Montgomery, Jr., J. A., & Thaddeus, P. 1974, *ApJ*, 193, L89
- Gregersen, E. M., Evans, II, N. J., Zhou, S., & Choi, M. 1997, *ApJ*, 484, 256
- Gueth, F., Bachiller, R., & Tafalla, M. 2003, *A&A*, 401, L5
- Gueth, F., Guilloteau, S., & Bachiller, R. 1996, *A&A*, 307, 891
- Gueth, F., Guilloteau, S., Dutrey, A., & Bachiller, R. 1997, *A&A*, 323, 943
- Hartmann, L., Calvet, N., & Boss, A. 1996, *ApJ*, 464, 387
- Hunter, C. 1977, *ApJ*, 218, 834
- Jørgensen, J. K., Schöier, F. L., & van Dishoeck, E. F. 2004, *A&A*, 416, 603
- Kirk, H., Johnstone, D., & Tafalla, M. 2007, *ApJ*, 668, 1042
- Kirk, J. M., et al. 2009, *ApJS*, 185, 198
- Kun, M. 1998, *ApJS*, 115, 59
- Kun, M., Kiss, Z. T., & Balog, Z. 2008, *Star Forming Regions in Cepheus*, ed. B. Reipurth, 136
- Kwon, W., Looney, L. W., Mundy, L. G., Chiang, H.-F., & Kemball, A. J. 2009, *ApJ*, 696, 841
- Lee, C.-F., Ho, P. T. P., & White, S. M. 2005, *ApJ*, 619, 948
- Lee, C. W., Myers, P. C., & Tafalla, M. 2001, *ApJS*, 136, 703
- Lee, J.-E., Bergin, E. A., & Evans, II, N. J. 2004, *ApJ*, 617, 360
- Li, A., & Draine, B. T. 2001, *ApJ*, 554, 778
- Looney, L. W., Mundy, L. G., & Welch, W. J. 2000, *ApJ*, 529, 477
- . 2003, *ApJ*, 592, 255
- Looney, L. W., Tobin, J. J., & Kwon, W. 2007, *ApJ*, 670, L131

- Mardones, D., Myers, P. C., Tafalla, M., Wilner, D. J., Bachiller, R., & Garay, G. 1997, *ApJ*, 489, 719
- Maret, S., Bergin, E. A., & Lada, C. J. 2006, *Nature*, 442, 425
- . 2007, *ApJ*, 670, L25
- Masunaga, H., & Inutsuka, S.-i. 2000, *ApJ*, 536, 406
- McKee, C. F., & Ostriker, E. C. 2007, *ARA&A*, 45, 565
- Miao, Y., Mehringer, D. M., Kuan, Y.-J., & Snyder, L. E. 1995, *ApJ*, 445, L59
- Momose, M., Ohashi, N., Kawabe, R., Nakano, T., & Hayashi, M. 1998, *ApJ*, 504, 314
- Myers, P. C., Fuller, G. A., Goodman, A. A., & Benson, P. J. 1991, *ApJ*, 376, 561
- Myers, P. C., Mardones, D., Tafalla, M., Williams, J. P., & Wilner, D. J. 1996, *ApJ*, 465, L133
- Natta, A., Testi, L., Neri, R., Shepherd, D. S., & Wilner, D. J. 2004, *A&A*, 416, 179
- Öberg, K. I., van Broekhuizen, F., Fraser, H. J., Bisschop, S. E., van Dishoeck, E. F., & Schlemmer, S. 2005, *ApJ*, 621, L33
- Offner, S. S. R., & Krumholz, M. R. 2009, *ApJ*, 693, 914
- Ohashi, N., Hayashi, M., Ho, P. T. P., & Momose, M. 1997a, *ApJ*, 475, 211
- Ohashi, N., Hayashi, M., Ho, P. T. P., Momose, M., Tamura, M., Hirano, N., & Sargent, A. I. 1997b, *ApJ*, 488, 317
- Ossenkopf, V., & Henning, T. 1994, *A&A*, 291, 943
- Pickett, H. M., Poynter, I. R. L., Cohen, E. A., Delitsky, M. L., Pearson, J. C., & Muller, H. S. P. 1998, *Journal of Quantitative Spectroscopy and Radiative Transfer*, 60, 883
- Saigo, K., Tomisaka, K., & Matsumoto, T. 2008, *ApJ*, 674, 997
- Sault, R. J., Teuben, P. J., & Wright, M. C. H. 1995, in *Astronomical Society of the Pacific Conference Series*, Vol. 77, *Astronomical Data Analysis Software and Systems IV*, ed. R. A. Shaw, H. E. Payne, & J. J. E. Hayes, 433
- Shirley, Y. L., Evans, II, N. J., Rawlings, J. M. C., & Gregersen, E. M. 2000, *ApJS*, 131, 249
- Shirley, Y. L., Nordhaus, M. K., Grcevich, J. M., Evans, II, N. J., Rawlings, J. M. C., & Tatematsu, K. 2005, *ApJ*, 632, 982
- Shu, F. H. 1977, *ApJ*, 214, 488

- Straizys, V., Cernis, K., Kazlauskas, A., & Meistas, E. 1992, *Baltic Astronomy*, 1, 149
- Tafalla, M., Myers, P. C., Caselli, P., Walmsley, C. M., & Comito, C. 2002, *ApJ*, 569, 815
- Tassis, K. 2007, *MNRAS*, 379, L50
- Tassis, K., & Mouschovias, T. Ch. 2005, *ApJ*, 618, 769
- Thaddeus, P., & Turner, B. E. 1975, *ApJ*, 201, L25+
- Tobin, J. J., Hartmann, L., Looney, L. W., & Chiang, H.-F. 2009, *ApJ*, submitted
- Tsamis, Y. G., Rawlings, J. M. C., Yates, J. A., & Viti, S. 2008, *MNRAS*, 388, 898
- Turner, B. E. 1974, *ApJ*, 193, L83
- Velusamy, T., Langer, W. D., & Goldsmith, P. F. 2002, *ApJ*, 565, L43
- Ward-Thompson, D., & Buckley, H. D. 2001, *MNRAS*, 327, 955
- Wilner, D. J., Myers, P. C., Mardones, D., & Tafalla, M. 2000, *ApJ*, 544, L69
- Wiseman, J., Wootten, A., Zinnecker, H., & McCaughrean, M. 2001, *ApJ*, 550, L87
- Womack, M., Ziurys, L. M., & Wyckoff, S. 1992, *ApJ*, 393, 188
- Zhou, S. 1992, *ApJ*, 394, 204
- Zhou, S., Evans, II, N. J., Koempe, C., & Walmsley, C. M. 1993, *ApJ*, 404, 232

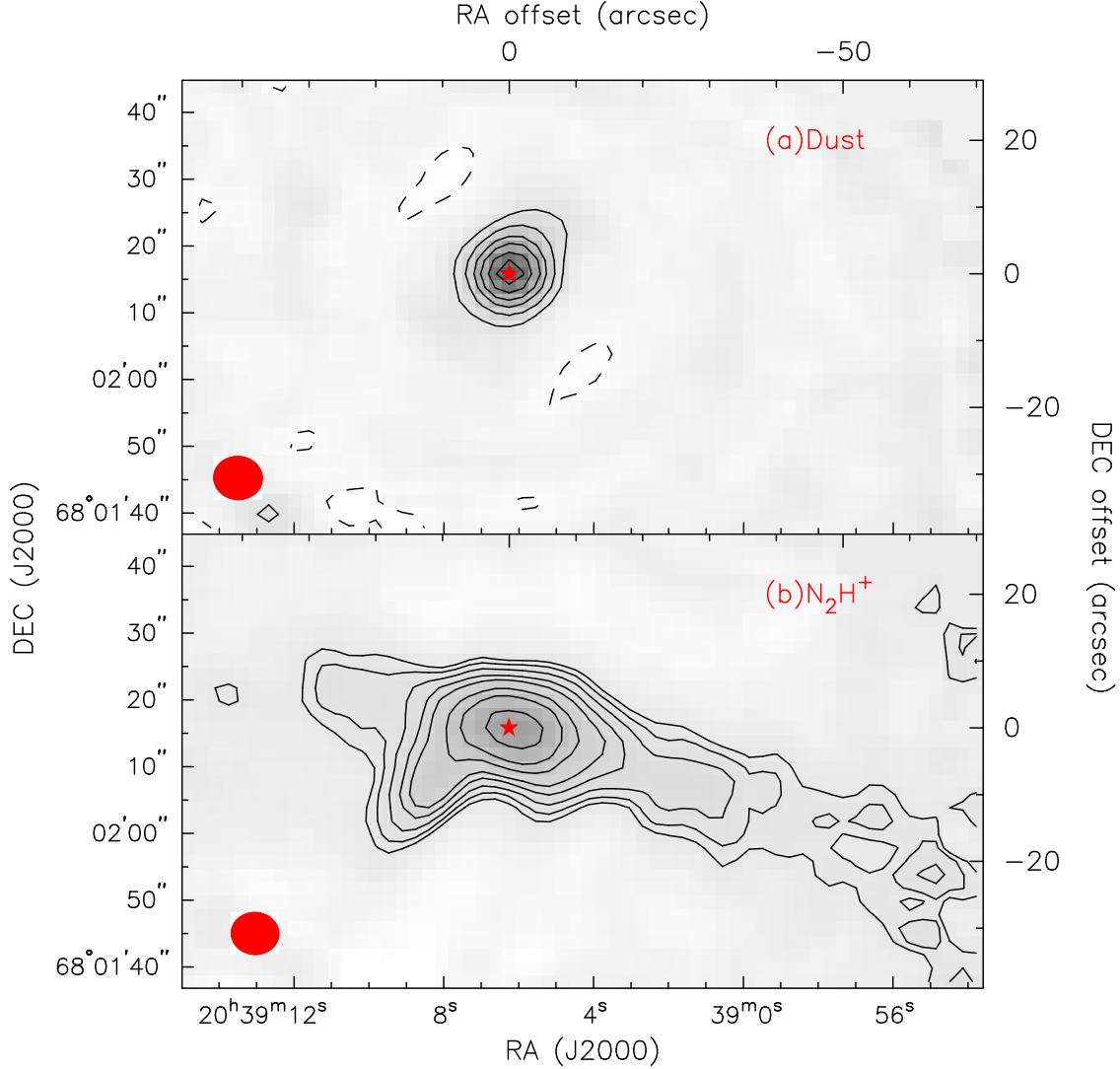


Fig. 1.— (a) 3 mm dust continuum of L1157 (*contours and gray scale*). The contour levels are  $[-2, 3, 6, 10, 14, 20, 26] \times \sigma$ , where  $\sigma = 1 \text{ mJy beam}^{-1}$  is the noise level, and the beam size is  $7.3'' \times 6.5''$  at a position angle of  $86.1^\circ$ . (b) The integrated intensity of  $N_2H^+$  over the isolated hyperfine component  $JF_1F=101-012$  ( $2.21\text{--}3.58 \text{ km s}^{-1}$ , *contours and gray scale*). The star marks the position of the central protostar. The contour levels are  $[3, 6, 10, 15, 20, 30, 40, 60, 80] \times \sigma$ , where  $\sigma = 0.01 \text{ Jy beam}^{-1} \text{ km s}^{-1}$ , and the beam size is  $7.1'' \times 6.3''$  at a position angle of  $86.6^\circ$ . Although negative contours exist due to the filtered-out large-scale structures, they are not plotted for simplicity.



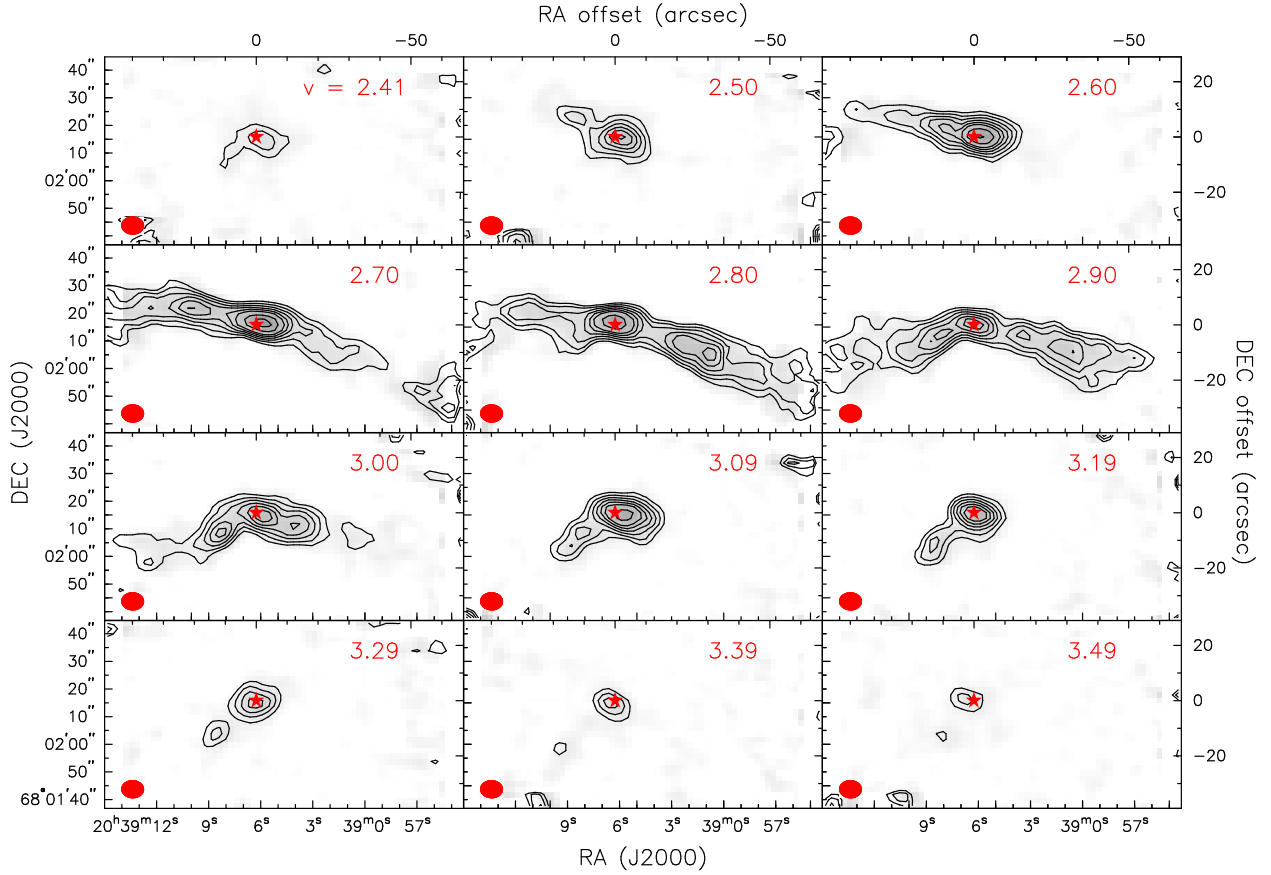


Fig. 2.— Channel maps of L1157 for the  $N_2H^+$   $JF_1F=101-012$  transition (*contours and gray scale*). The numbers in the upper-right corner are the LSR velocity for each channel. The star marks the position of the central protostar. The contour levels are  $[2, 3, 4, 5, 6, 7, 9, 11] \times \sigma$ , where  $\sigma = 0.08 \text{ Jy beam}^{-1}$ , and the beam size is  $7.1'' \times 6.3''$  at a position angle of  $86.6^\circ$ . Negative contours are not plotted for simplicity.

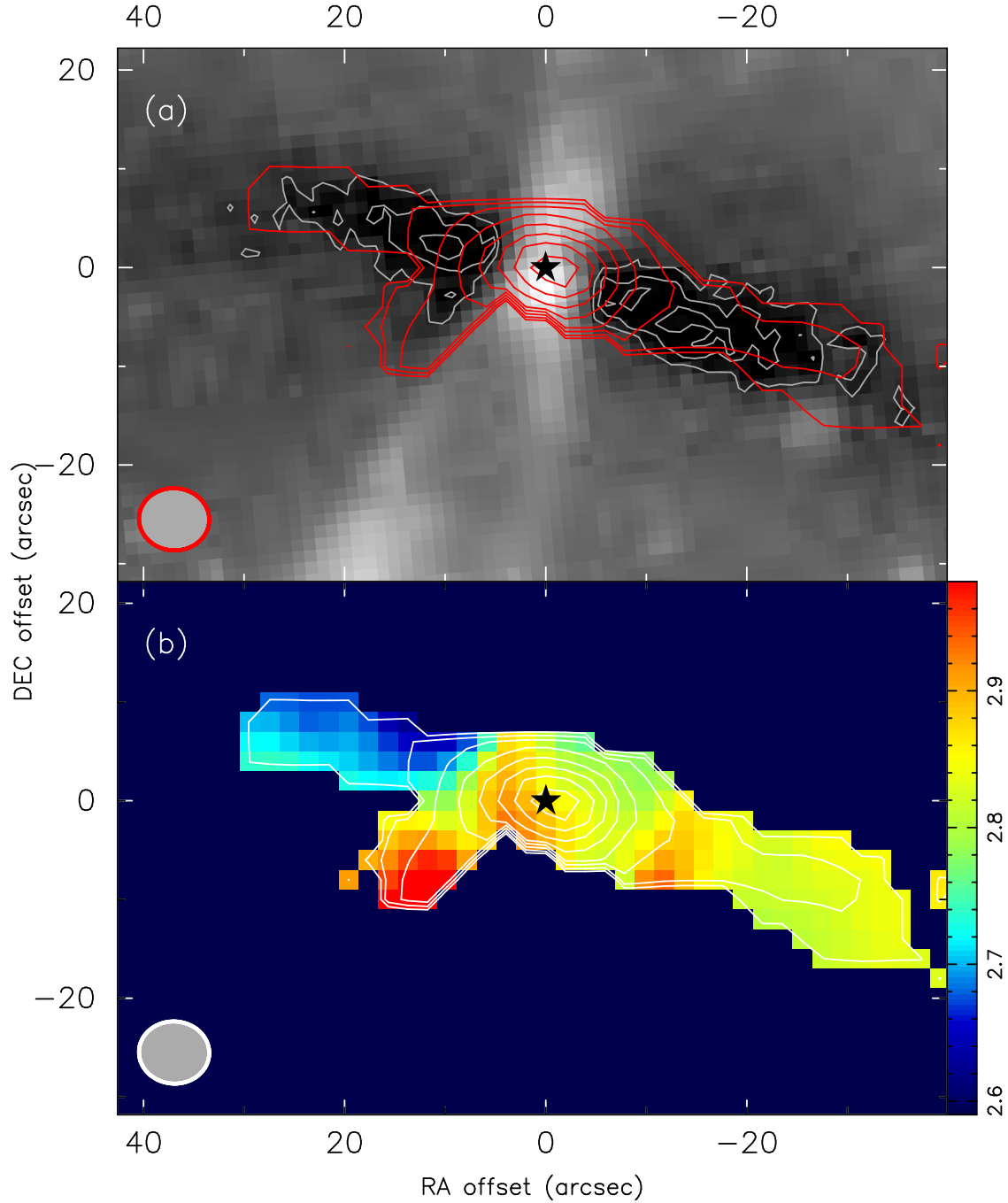


Fig. 3.— (a) IRAC 8  $\mu\text{m}$  image of L1157 (Looney et al. 2007, *grayscale and gray contours*) overlaid with  $\text{N}_2\text{H}^+$  column density (*red contours*) derived from the CARMA observations. The star marks the position of the protostar. The (*red*) contour levels for the  $\text{N}_2\text{H}^+$  column density are  $[0.1, 0.5, 1.0, 1.5, 2.0, 2.5, 3.0, 3.5] \times 10^{13} \text{cm}^{-2}$  (see the text for discussion of uncertainty); and the (*gray*) contours showing the absorption features are  $[7, 8, 9, 10] \times \sigma$ , where  $\sigma = 0.042 \text{ MJy}^{-1} \text{sr}^{-1}$  is the noise level. The circle at the lower-left corner shows the beam size of the CARMA observations. (b) Velocity map ( $v_{\text{LSR}}$ ) overlaid by the column density contours from (a), both derived from the CARMA observations of the  $\text{N}_2\text{H}^+$  flattened envelope.

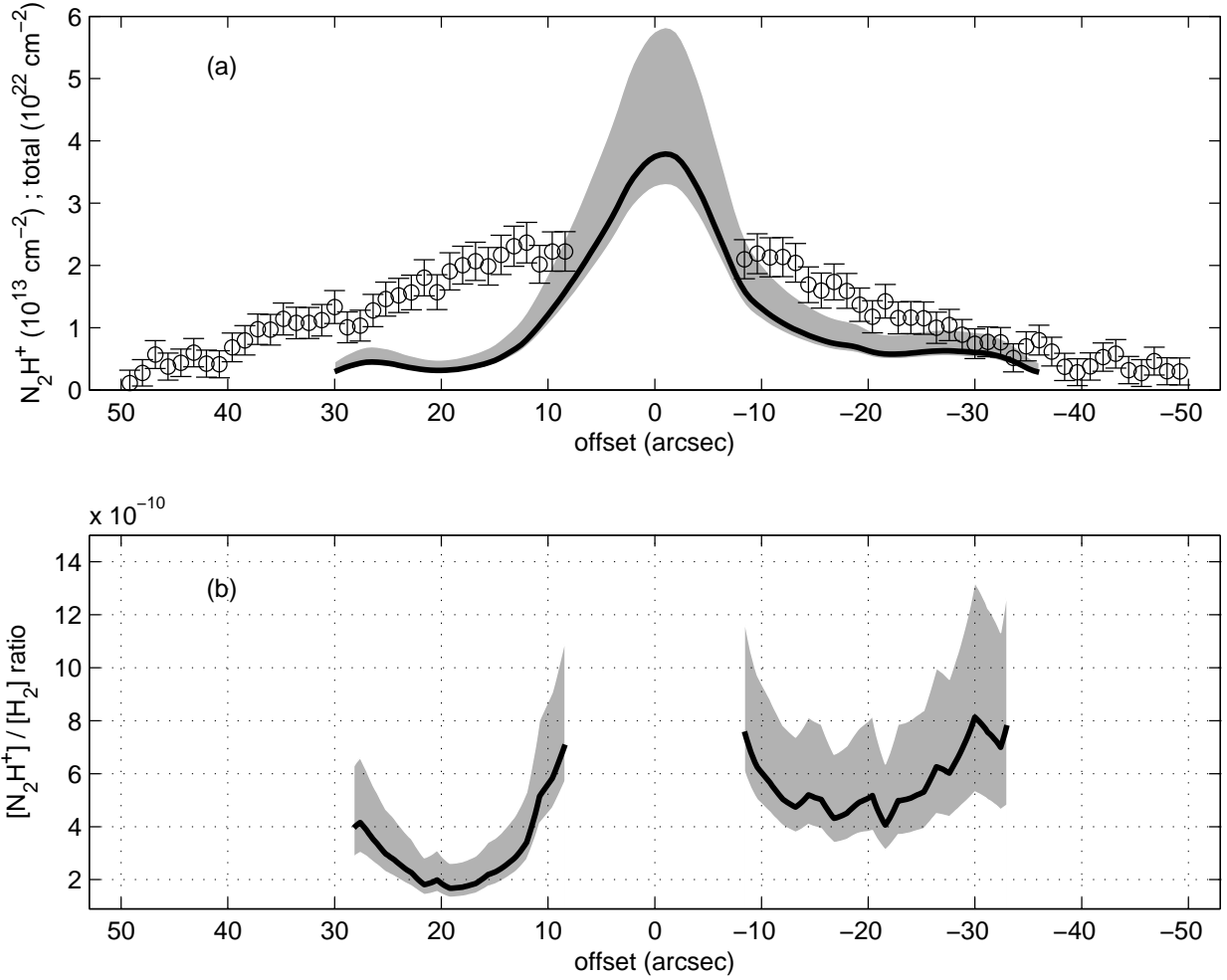


Fig. 4.— (a) Column density of  $\text{N}_2\text{H}^+$  (from our CARMA observation, *curve with shading*) and total gas plus dust (from *Spitzer* observation, *circles with error bars*) along the major axis of the extended envelope. (b)  $\text{N}_2\text{H}^+$  abundance profile by taking the ratio of  $[\text{N}_2\text{H}^+]$  and  $[\text{H}_2]$  from the CARMA observations and 8  $\mu\text{m}$  absorption feature. The shaded region shows the uncertainty.

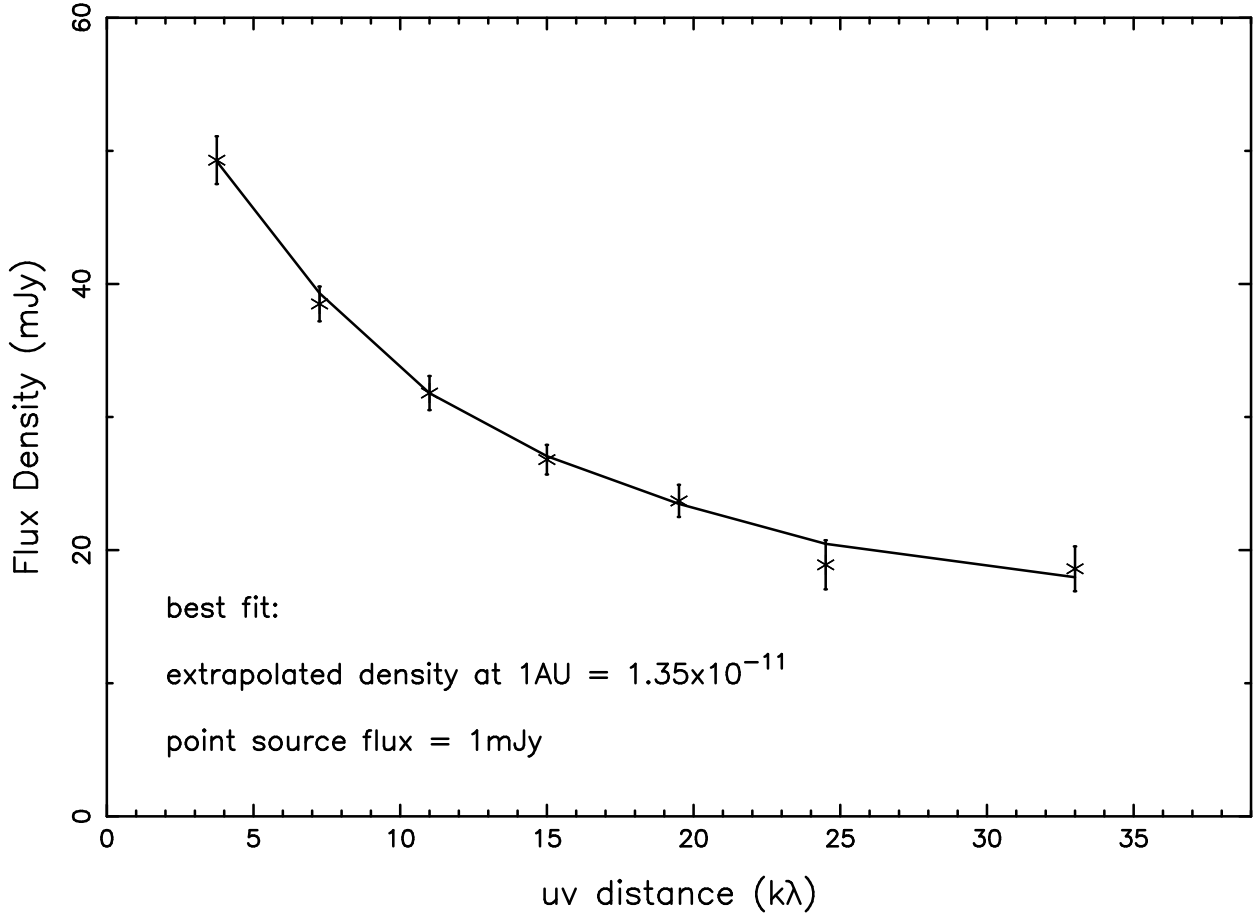


Fig. 5.— Annuli-averaged flux density for the 3mm dust continuum of L1157 (*crosses with error bars*). The curve show the best-fit model binned in the same fashion. The dust model has a power-law density profile with index = -2 tapered by a vertical Gaussian with a scale height of 2000AU. The extrapolated density at 1AU is  $1.35 \times 10^{-11} \text{ g cm}^{-3}$  and an unresolved point source flux of 1mJy is added. The inner radius of the envelope is 5AU, and the outer radius is 15000 AU. The reduced  $\chi_r^2$  is 0.225 for this best-fit model.

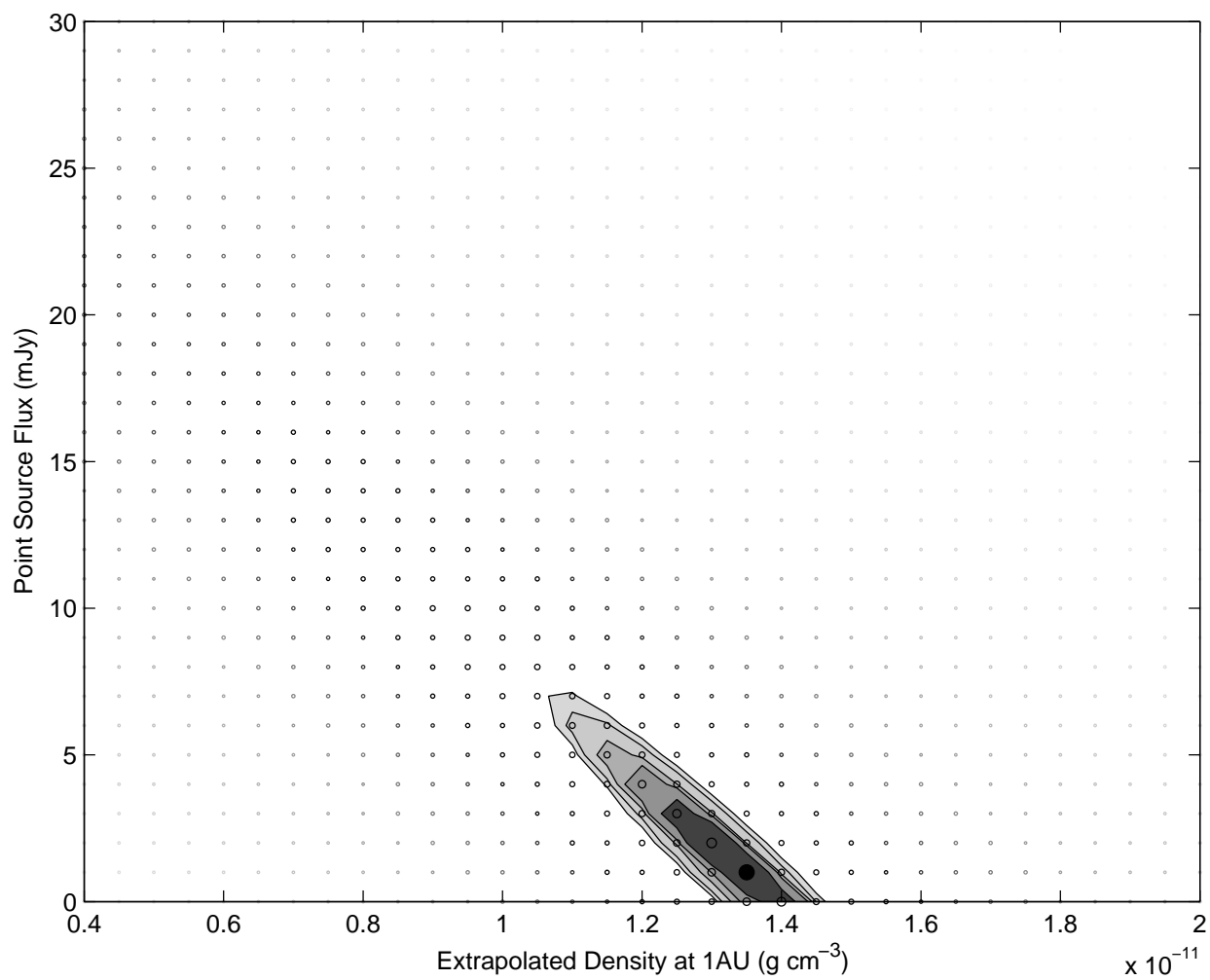


Fig. 6.— Summary of the dust continuum fits. Circles show the grid of models with sizes and shades representing the goodness of fits. Contours are confidence levels of 99%, 95%, 90%, 80%, and 50%. The filled circle at  $1.35 \times 10^{-11} \text{g cm}^{-3}$  and 1 mJy is the best fit.

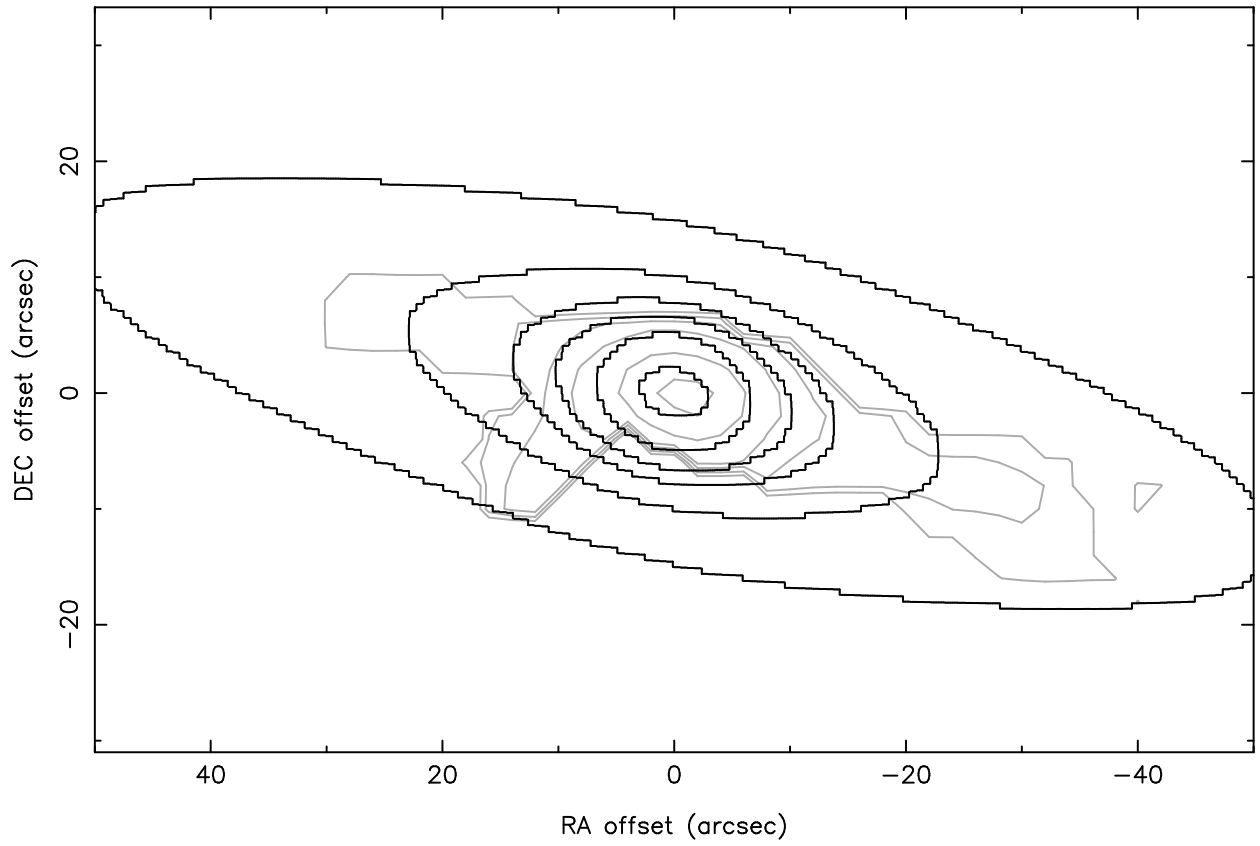


Fig. 7.—  $N_2H^+$  column density of the best-fit model by dust continuum modeling (*black contours*) and observations (*grey contours*). The contour levels (for both) are  $[0.1, 0.5, 1.0, 1.5, 2.5, 3.5] \times 10^{13} \text{cm}^{-2}$ . The depletion effect is taken into account at the central region where the density is above  $1.5 \times 10^6 \text{cm}^{-3}$ .

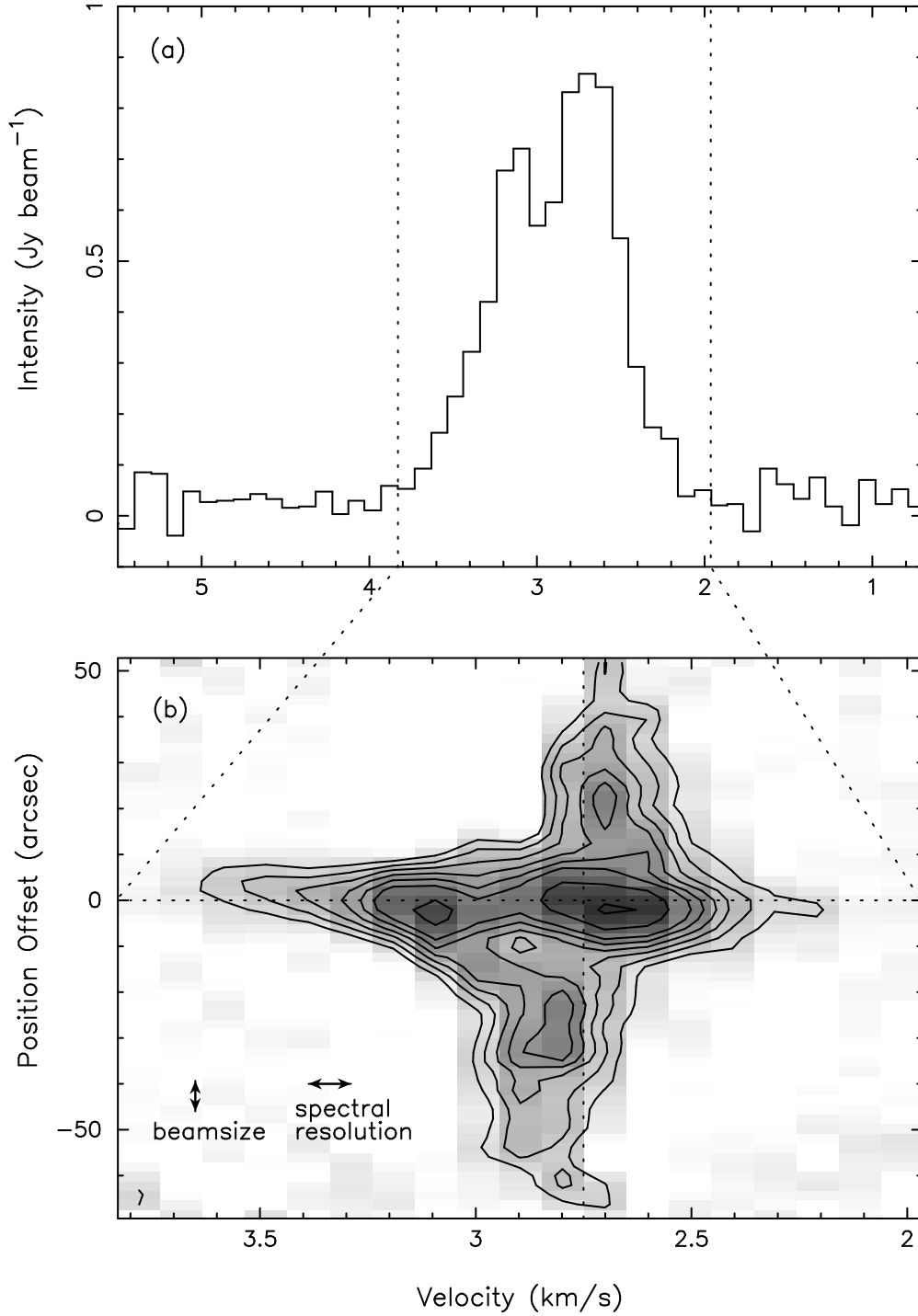


Fig. 8.— (a) Spectrum of the  $\text{N}_2\text{H}^+$   $JF_1F=101-012$  line at the location of the protostar. (b) Position–velocity diagram of the  $\text{N}_2\text{H}^+$   $JF_1F=101-012$  line along the major axis of the flattened envelope feature, a slice with position angle of  $75^\circ$ . The contour levels are  $[2, 3, 4, 5, 6, 7, 9, 11] \times \sigma$ , where  $\sigma = 0.08 \text{ Jy beam}^{-1}$ . The angular and spectral resolutions of observations are shown, and the pixel size of the gray scale is the interferometric imaging cell size.

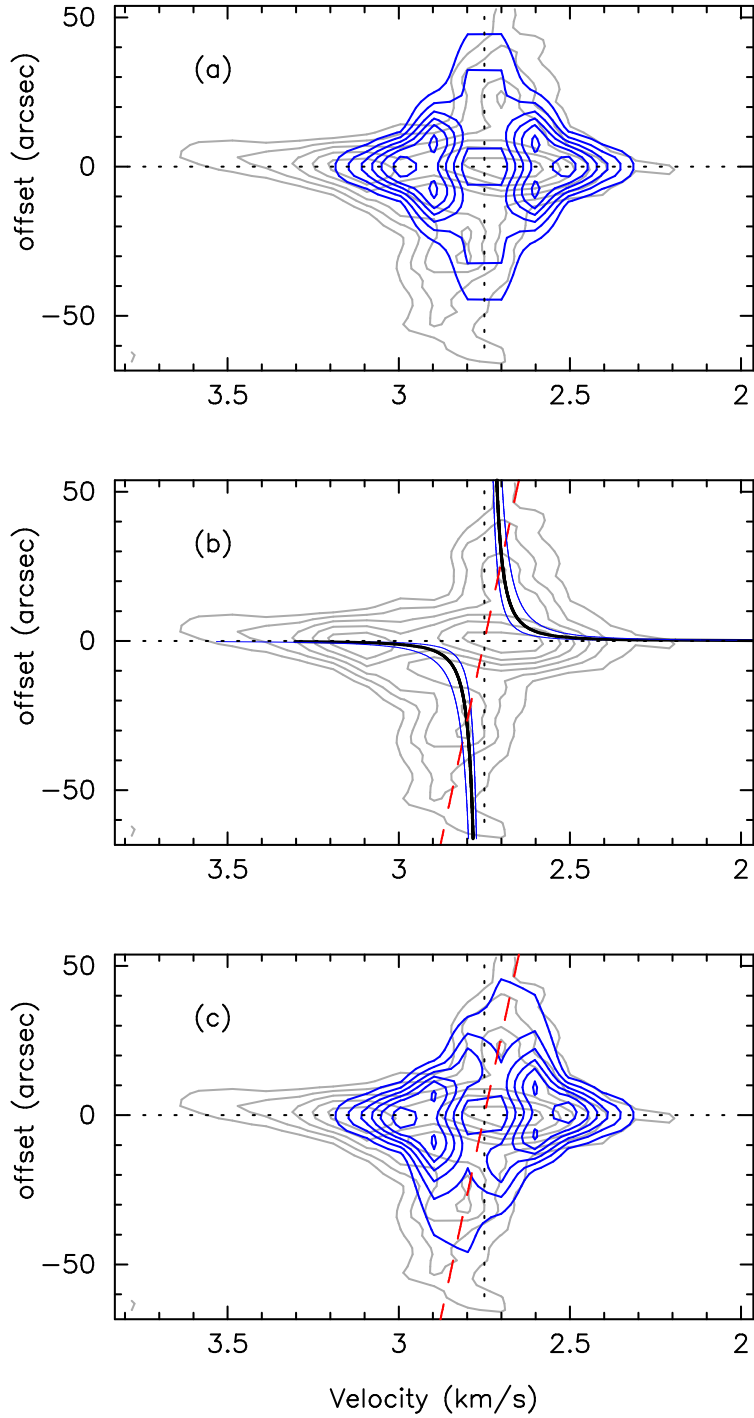


Fig. 9.— Observed (*gray contours*) and model (*blue contours*) PV diagrams for the flattened envelope of L1157: (a) pure infall motion, (b) solid curves show the point-mass Keplerian rotation for  $M_{\star}=0.01, 0.02,$  and  $0.04 M_{\odot}$ , dashed line shows solid-body rotation with angular velocity of  $1.5 \text{ km s}^{-1} \text{ pc}^{-1}$ , and (c) combined model of infall plus solid-body rotation.



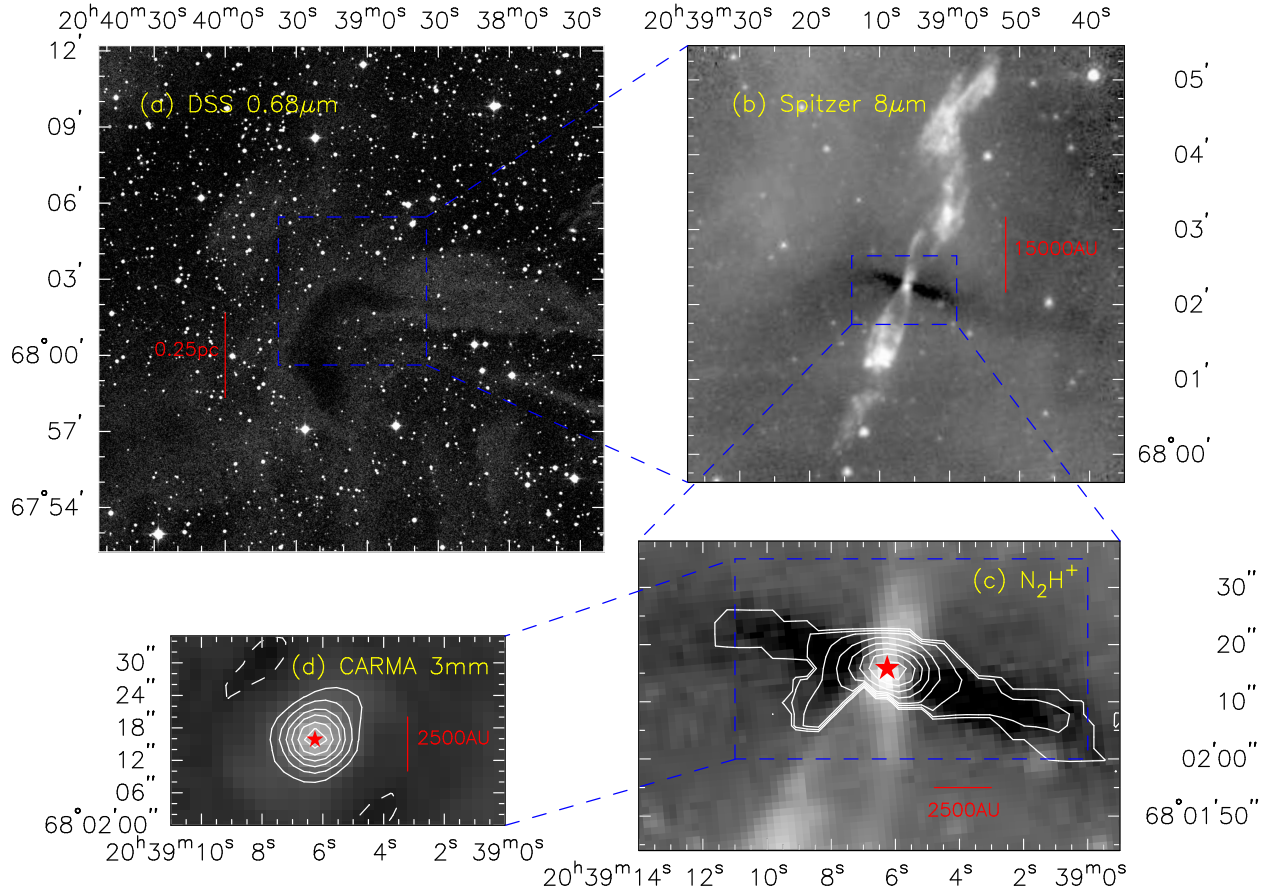


Fig. 10.— L1157 at different scales seen by various observations: (a) DSS optical image, (b) *Spitzer* IRAC 8  $\mu\text{m}$  image, (c) zoomed-in 8  $\mu\text{m}$  image overlaid with the  $\text{N}_2\text{H}^+$  column density map, (d) 3 mm dust continuum observed by CARMA. Different geometric characteristics are shown. The cloud is irregular at scale of  $\sim 0.5$  pc, flattened perpendicular to the outflows at scale of  $\sim 15,000$  AU, and nearly spherical at size scales smaller than  $\sim 5,000$  AU.

Table 1. Summary of 3 mm Dust Continuum

Parameter	Value
Peak flux density (mJy beam <sup>-1</sup> )	30.3
Noise level $\sigma$ (mJy beam <sup>-1</sup> ) . . . .	1.0
Total flux density (mJy) . . . . .	48.3 $\pm$ 0.7
Gaussian fit	
Major axis (arcsec): . . . . .	9.4 $\pm$ 0.9
Minor axis (arcsec): . . . . .	8.1 $\pm$ 0.4
Position angle (degree) . . . . .	-68 $\pm$ 18
Deconvolved Size	
Major axis (arcsec) . . . . .	6.1 $\pm$ 2.3
Minor axis (arcsec) . . . . .	4.4 $\pm$ 0.8
Position angle (degree) . . . . .	-54 $\pm$ 21

Note. — The results of Gaussian fit with the dust continuum done by the MIRIAD task IMFIT.

Table 2. Summary of N<sub>2</sub>H<sup>+</sup> Spectrum Fitting

Parameter	Central Pixel	Mean Value	Mean $\sigma$
$v_{\text{LSR}}$ (km s <sup>-1</sup> )	2.85	2.82	0.02
$\Delta v$ (km s <sup>-1</sup> )	0.80	0.44	0.03
$\langle \tau \rangle$	0.63	0.31	0.03
Derived values :			
Column density(10 <sup>12</sup> cm <sup>-2</sup> )	38.3	9.7	3.2